Probabilistic estimation of glacier surface elevation changes from DEM differentiation: a Bayesian method for outlier filtering, gap filling and uncertainty estimation with examples from High Mountain Asia

Grégoire Guillet [1], **Tobias Bolch** [1]

[1]School of Geography and Sustainable Development, University of St-Andrews

St Andrews, Scotland, United Kingdom of Great Britain and Northern Ireland

Key Points:

- Probabilistic surface elevation change estimates are consistent with previously published ones while not producing similar artifacts
- Bayesian framework allow to unify outlier filtering, void filling and uncertainty estimation within a statistically coherent framework.
- Results highlight the need to consider glacier dynamics when processing glacier surface elevation change datasets

Corresponding author: Grégoire Guillet, gg70@st-andrews.ac.uk

Abstract

Various interdisciplinary studies have shown substantial discrepancies between modeled and remotely sensed glacier surface elevation change. It is therefore crucial to better understand and quantify uncertainties associated to both methods. We design a probabilistic framework with the aim to filter outliers, fill data voids and estimate uncertainties in glacier surface elevation changes computed from Digital Elevation Model (DEM) differentiation. The technique is based on a Bayesian formulation of the DEM difference problem and specifically targets surging and debris-covered glaciers, both at glacier and regional scales. We first define a set of physically admissible surface elevation changes as an elevation-dependent probability density function. In a second step, terrain roughness is defined as the main descriptor for DEM uncertainty. Each surface elevation change pixel is a probability distribution. We present validation experiments in High Mountain Asia and show that the model produces results consistent with conventional DEM differencing, while avoiding the caveats of already existing methods. We further demonstrate that accounting for unstable glacier dynamics is crucial for accurate outlier filtering and robust uncertainty estimation. The technique can be applied to other types of remotely sensed glacier quantities (surface velocity etc.) and so would help to improve the characterization of uncertainty associated with changes in glacier mass and dynamics.

Plain Language Summary

Glacier volume changes are traditionally studied by subtracting datasets representing the elevation of a glacier's surface at different time periods. These datasets, called digital elevation models, are generated by various algorithms from images acquired by air- and space-borne sensors. Digital elevation models are thus inherently erroneous representations of the true and unknown ground surface elevation. Errors in elevation will ultimately generate incorrect values of glacier volume change that need to be filtered out. Most methods used to filter incorrect signal in glacier surface elevation changes rely on statistical thresholds, without using available knowledge on glacier physics. In this paper, we present a novel method to filter incorrect values and provide a measurement of the uncertainty associated with glacier volume changes. This is done by evaluating how likely the observed volume changes are, given what is already known about glacier physics. More specifically we compare the computed glacier volume change with a set of admissible values defined by the glacier's parameters and flow regime. We test the proposed methodology against already published results and find that existing caveats are eliminated from our results. We further demonstrate the need to account for a glacier's flow regime when dealing with volume change datasets.

1 Introduction

The increasing collection of surface elevation datasets has created a vast archive of snapshots for the study of land ice. Digital elevation datasets have now become ubiquitous in the study of glaciers (Wheate et al., 2014; Falaschi et al., 2019; King et al., 2021), ice caps (Bingham & Rees, 1999; Moholdt & Kääb, 2012; Papasodoro et al., 2015) and ice sheets (Davis & Ferguson, 2004; Whitehead et al., 2013; Shean et al., 2019; Simonsen et al., 2021) and present a large potential to further our understanding of ice dynamics, cryosphere/climate relationships and future sea level rise (Gardner et al., 2012). Lately, efforts have primarily focused on producing new, more accurate digital elevation models (DEMs) from air- and space-borne optical or radar sensors (Muskett et al., 2009; Neckel et al., 2014; Moholdt & Kääb, 2012; Leinss & Bernhard, 2021), declassified imagery (Kim et al., 2007; Dehecq et al., 2020) and state-of-the-art processing techniques (Noh & Howat, 2015; Mertes et al., 2017; Mölg & Bolch, 2017; Bhushan et al., 2021; Janowski et al., 2021). In parallel, studies have used the generated elevation datasets to quantify glacier changes

over longer timescales (Bolch et al., 2011; Bhattacharya et al., 2021; King et al., 2020), broader spatial scales (Hugonnet et al., 2021) and with higher temporal and spatial resolution (Aizen et al., 2006; Brun et al., 2016, 2017; Jakob et al., 2021).

The various DEMs used to compute glacier surface elevation changes are often of uneven quality as many originate from different sensors (Toutin, 2008; González-Moradas & Viveen, 2020), are processed using different algorithms (Futamura et al., 2002; Beyer et al., 2018; Bhushan et al., 2021), have inconsistent spatial resolutions (Bolch et al., 2008; Bhattacharya et al., 2021) or are affected by clouds (Bolch et al., 2005), among others. These limitations can introduce substantial bias and uncertainties in the information derived from glacier surface elevation changes compute by differencing two or more DEMs (Paul, Bolch, et al., 2017; Podgórski et al., 2019). Example of typical biases are erroneous elevation measurements resulting from radar penetration in radar DEMs (Gardelle et al., 2012), and data voids (or anomalous values) resulting from weather or illumination conditions (Kaab, 2008; Bris & Paul, 2015; Paul, Bolch, et al., 2017) as well as tilts or along/cross track biases in DEMs derived from optical sensors (Girod et al., 2017), among others.

Mitigating biases on the information derived from DEM differences has been the focus of substantial efforts in the past decades. While the state-of-the-art co-registration method proposed by Nuth and Kääb (2011) has now become standard for eliminating DEM shifts, elevation biases and higher-order sensor specific biases, a wide variety of outlier filtering, gap filling and uncertainty estimation methods are used in individual studies (Gardelle et al., 2013; Pieczonka et al., 2013; Pieczonka & Bolch, 2015; Shangguan et al., 2015). More often than not, such methods rely on the implicit assumption that glacier surface elevation changes are normally distributed over the study area. While reasonable at a global scale, this assumption is likely to be invalid at regional and glacier scales, especially in regions where a substantial part of the glacierized area is affected by surges or debris-covered.

Unstable glacier dynamics (glaciers surges) and extensive debris cover can indeed heavily alter the mass balance signal, both at glacier and regional scales (Vincent et al., 2016; Vijay & Braun, 2018). In regions where surge-type or debris-covered glaciers are numerous, such as High Mountain Asia where surge-type glaciers represent $\approx$ 20% of the glacierized area ($\approx$ 50% in the Karakoram, see Bhambri et al. (2017); Guillet et al. (2021) for more), the assumption of normality for surface elevation changes is thus unlikely to be valid, making standard outlier filtering methods unreliable. Accounting for potential unstable dynamics or debris cover in the DEM differencing process and providing a quantification of the uncertainties on the surface elevation changes is crucial. Furthermore, given the widespread use of surface elevation changes, and by extension geodetic mass balance, in different operations (Mayr et al., 2013; Duethmann et al., 2015), keeping track of uncertainties and how they propagate through the chain of operations is primordial.

In this paper, we present a method aiming at addressing both the outlier filtering/gap filling and uncertainty estimation problems. We here aim to define a unified framework to derive glacier surface elevation changes, based on a probabilistic formulation of DEM differentiation. The method is specifically designed for contexts where the presence of surge-type or debris-covered glaciers might alter the surface elevation signal. The outlier filtering and gap filling problems are here seen as a Bayesian inference problem, where we aim at providing the probability distribution of glacier surface elevation change, given previous knowledge on glacier dynamics and error modeling. By unifying the DEM differencing problem with simple glacier elevation changes modeling within a statistically consistent framework we further aim to provide estimation of the uncertainty on glacier surface elevation changes.

2 The DEM differentiation problem: uncertainties and Bayesian formulation

2.1 Errors and uncertainties in elevation data

Digital elevation models are inherently imperfect representations of the true ground surface. Errors, or deviations of the data from the true ground surface elevation, are traditionally defined as either gross, systematic or random. While gross errors, or blunders, originate from equipment failure and are thus unlikely in commercial elevation data sets, many systematic errors have been documented in state-of-the-art commercial datasets (Jacobsen, 2016; Nikolakopoulos, 2020). Examples include both planimetric (XY) and vertical (Z) spurious pixel, line and edge effects as well as pits and spikes; all resulting from the DEM production process. Random errors typically also arise from the editing and processing steps, and represent random variations around the true ground surface elevation.

More formally, the relationship between a DEM ($\tilde{Z}$) and the true surface elevation map it represents can be described as follows :

$$\tilde{Z} = Z + \epsilon \tag{1}$$

where $\tilde{Z}$ is the imperfect representation of the true and unknown elevation Z and ϵ quantifies all the errors associated to each elevation measurement.

Deviations between $\tilde{Z}$ and Z are often described using simple metrics, the most common descriptor being the root mean squared error (RMSE), for which estimates are usually provided in the DEM documentation:

$$RMSE := \sqrt{\frac{1}{n}\Sigma_{i=1}^{n}\left(\tilde{Z}_i - Z_i\right)^2} \tag{2}$$

Global error metrics however fail to fully characterize DEM errors (Liu & Jezek, 1999; Carlisle, 2005; Erdoğan, 2010). DEM errors have been shown to vary spatially, and to correlate with various local terrain properties, most notably terrain ruggedness (Kyriakidis et al., 1999), slope and local elevation (Liu & Jezek, 1999; Aguilar et al., 2005). Furthermore, as the true real-world ground surface elevation (Z) is inaccessible, DEM errors themselves are thus known up to a certain level of certainty. Considering that neither the true ground surface elevation map Z, nor the true error map ϵ can be derived from realizations of $\tilde{Z}$, we here propose to formulate $\tilde{Z}$ as a range of values within which one can expect Z to lie, with a certain level of certainty rather than a single value estimate affected by errors.

2.2 DEM differencing and uncertainty quantification in glaciology

Among change detection methods, DEM differencing to produce DEMs of difference (DoDs) is the most widespread in glaciology. Prior to being subtracted, two DEMs of the same study area are traditionally co-registered. Co-registration is a widespread processing step aiming at spatially aligning two (or more) elevation datasets. Features present on both datasets should overlap as well as possible after co-registration. Perfect match between the co-registered datasets is however unlikely. In glaciological applications, misalignment of data sets may result in erroneous interpretation of surface elevation changes leading to false identification of surge-type dynamics or incorrect estimations of glacier volume changes, for example. Further details on the co-registration procedure can be found for example in Nuth and Kääb (2011); K. Wang and Zhang (2015).

From Eq. 1, one can formulate the difference between two co-registered elevation data sets acquired at different times (with $t > t_0$) as follows:

$$\begin{aligned}\tilde{\Delta h} &= \tilde{Z}_t - \tilde{Z}_{t_0} \\ &= Z_2 - Z_1 + (\epsilon_t - \epsilon_{t_0}) \\ \tilde{\Delta h} &= \Delta h + \epsilon_{\Delta h}\end{aligned} \tag{3}$$

where $\tilde{\Delta h}$ is the inexact representation of the elevation difference between the data sets, Δh is the true and unknown elevation difference and $\epsilon_{\Delta h}$ is the associated ill-constrained error. Δh conveys the geophysical signal of surface elevation change. As surface elevation changes in glaciers can be the consequence of a wide spectrum of phenomena, providing a robust estimate of Δh (i.e. $\tilde{\Delta h}$) is crucial. Common approaches to estimating Δh require filtering outliers from the computed DoD before filling potential gaps and estimating $\epsilon_{\Delta h}$.

2.2.1 Filtering of outliers and gap filling

Outlier filtering refers to the process of identifying and removing pixels with non-physical Δh values. Outliers in DoDs originate, for example, from the presence of clouds on one of the DEMs or in zones shadowed by adjacent topography.

A widespread method for outlier filtering consists in assuming that $\tilde{\Delta h}$ follows a Gaussian distribution centered around a mean $\mu_{\tilde{\Delta h}}$ with standard deviation $\sigma_{\tilde{\Delta h}}$. Any $\tilde{\Delta h}$ satisfying $|\tilde{\Delta h}| \geq 3{*}\sigma_{\tilde{\Delta h}}$ is considered an outlier and filtered (Gardelle et al., 2013). While the normality assumption is often reasonable, the distribution of $\tilde{\Delta h}$ is likely to be skewed or present heavy tails (Kargel et al., 2014; Nilsson et al., 2015), if, for example, a substantial numbers of glaciers in the study area display surge-type behavior or an extensive debris cover (see section 2.3.2 for further details). Furthermore, both $\mu_{\tilde{\Delta h}}$ and $\sigma_{\tilde{\Delta h}}$ are corrupted by outliers.

As a substitution to standard statistics-based outlier filtering methods, D. Wang and Kääb (2015) proposed to bound admissible elevation change values between user-defined extrema. They typically assume Δh to lie within a non-symmetrical interval ($[-30, 10]m{*}a^{-1}$ for example), as glacier thickening is not believed to exceed maximum precipitation and is likely to be outbalanced by thinning. While bounding admissible Δh values produced reliable results within the tDEM framework proposed by D. Wang and Kääb (2015), it is however restricted to the study of glaciers displaying stable dynamics. The more complex surface elevation change patterns encountered, for example, in the presence of surging glaciers (see Section 2.3.2 for more) requires different filtering approaches.

To account for potentially extreme $|\tilde{\Delta h}|$ values originating from unstable glacier dynamics, Pieczonka and Bolch (2015) proposed a non-linear elevation-dependent filter. Their method relies on weighting the standard deviation of $\tilde{\Delta h}$ ($\sigma_{\tilde{\Delta h}}$) by a rectangular function computed in few steps. The major shortcoming of this filter originates from the normalization process depicted by the authors in Equation E1. The computed w is not a normalized value bounded between $[0, 1]$ and rather $w \in [0, \infty]$ and thus shows high variability with glacier size. This leads to saturate the hyperbolic (tangent) function used in Equation E2, and thus to an increase in the number of Δh values close to 0, for glaciers with low elevation difference. Furthermore, as pointed out by the authors, the standard deviation $\sigma_{\tilde{\Delta h}}$, used to test whether a given $\tilde{\Delta h}$ is an outlier, is corrupted by anomalous values and therefore not robust to outliers.

Gap filling here refers to the process of imputing values to missing DoD pixels using mathematical interpolation techniques. In the following, we briefly describe the most commonly used methods in GIS-based applications: inverse distance weighting (IDW) and kriging. For a more in-depth review of void interpolation methods and their applicability in glaciology, we refer the reader to the works of McNabb et al. (2019).

196 *2.2.1.1 Inverse Distance Weighting (IWD)* IWD is a deterministic interpolation
197 method that computes the weighted average of observed values within the neighborhood
198 of a given target point. The pixels in the vicinity of the target pixel carry heavier weights
199 than more distant ones, with rate of weight decay being controlled by a power param-
200 eter. Considering the unknown Δh value at pixel p, one can compute $\tilde{\Delta h}_p$ as:

$$\tilde{\Delta h}_p = \frac{\sum_{i=1}^{n} \left(\frac{\tilde{\Delta h}_i}{d_i^{\beta}} \right)}{\sum_{i=1}^{n} \left(\frac{1}{d_i^{\beta}} \right)} \tag{4}$$

201 where n represents the number of pixels in the vicinity of the target pixel p, d_i is
202 the distance between pixel i and the target pixel and β is the power parameter. Typ-
203 ical values of β range from 1 to 4, with $\beta = 2$ being the most common and providing
204 the inverse distance-squared interpolator.

205 While IWD is an intuitive and computationally inexpensive method, it suffers from
206 a number of drawbacks (Li & Heap, 2014). The choice of the power parameter β and the
207 number of neighboring points n is often arbitrary even if methods such as cross-validation
208 can provide insight on these parameters. IWD is deterministic as the algorithm relies
209 on distances and thus does not provide any estimation of the uncertainty associated to
210 the prediction. Finally, predictions provided by IWD are sensitive to outliers as well as
211 observation sampling.

212 *2.2.1.2 Kriging* Kriging is a spatial interpolation technique similar to IWD as
213 it is a linear estimator aiming at predicting an unknown function value (in this partic-
214 ular case, surface elevation change on a DEM) at a target point as the weighted aver-
215 age of neighboring known values. Many variants of Kriging have been developed over
216 the years (Weng, 2006; Li & Heap, 2014). In the present case we will only discuss Or-
217 dinary Kriging (OK), as it is the most widely used variant in geoscientific applications.
218 The main difference between OK and IDW lies in the process of weight estimation, as
219 OK ensures minimum estimation variance given a specified spatial autocorrelation (var-
220 iogram or other characterization of the spatial covariance or correlation).

221 OK is a more sophisticated linear estimator than IWD. It however presents sim-
222 ilar drawbacks as it does not allow for prediction uncertainty quantification and is af-
223 fected by potential skewness of the data (Li & Heap, 2014). Indeed, in cases involving
224 spatially concentrated extreme values (surge-type glaciers actively surging for example),
225 a crude estimation of the mean using a linear estimator will lead to instability in esti-
226 mated values. Furthermore, as the data distribution is likely skewed, the mean is not an
227 appropriate descriptor of an average value of the distribution.

228 ***2.2.2 Estimation of glacier surface elevation change uncertainties***

229 Once outliers have been removed and gaps filled, a common strategy to estimate
230 Δh from realizations of $\tilde{\Delta h}$ is to evaluate the associated error $\epsilon_{\Delta h}$. While there is no best
231 method to do so, error analysis frameworks have been proposed to provide the best pos-
232 sible estimate of $\epsilon_{\Delta h}$ in glaciological applications. The standard deviation of $\tilde{\Delta h}$ over
233 stable non-glacierized terrain is often used as first estimate. More recently, Gardelle et
234 al. (2013) assumed that the $\epsilon_{\Delta hi}$ associated to each elevation change pixel $\tilde{\Delta hi}$ within
235 an elevation band equals the standard deviation of the band's $\tilde{\Delta h}$ ($\sigma_{\tilde{\Delta h}}$) up to a coef-
236 ficient depending on the spatial autocorrelation (see Equation 2 in Gardelle et al. (2013)).
237 As discussed by the authors, $\sigma_{\tilde{\Delta h}}$ not only captures the uncertainty associated to $\tilde{\Delta h}$ but
238 also conveys the natural variability of surface elevation change in the corresponding el-
239 evation band. Furthemore, this formulation only accounts for one-dimensional (band-

wise, see Bretherton et al. (1999)) uncertainty and is not suited for 2-dimensional datasets (Dehecq et al., 2020).

In the present paper, we propose a different uncertainty estimation strategy. We rely on a probabilistic formulation of the DEM differencing operation to unify the outlier filtering, gap filling and uncertainty modeling problems in a statistically coherent framework. We here aim to infer a distribution of values of Δh, compatible with a set of given $\tilde{\Delta h}$ and knowledge on glacier dynamics. Instead of producing a single point estimate for Δh, we obtain a probability density function for each pixel of any considered DoD. The probability density function is conditional on the observed surface elevation change (See Section 2.3.1), and any prior information on probable values of Δh (See Section 2.3.2).

2.3 Bayesian formulation

Let us consider the DEM differentiation problem for two co-registered DEMs for which we compute $\tilde{\Delta h}$ (as described in Equation 3). We note I any information available about Δh known before considering $\tilde{\Delta h}$, called prior information. I here mainly includes assumptions about glacier dynamics (stable or unstable). The Bayesian DEM differentiation problem amounts to finding $P(\Delta h|\tilde{\Delta h}, I)$ which is the probability density of Δh conditional to knowing both $\tilde{\Delta h}$ and I also known as the *posterior* probability density function (PDF) of Δh. More formally, applying Bayes' theorem to our problem, we can write:

$$P(\Delta h|\tilde{\Delta h}, I) = \frac{P(\tilde{\Delta h}|\Delta h, I)P(\Delta h|I)}{P(\tilde{\Delta h}|I)} \tag{5}$$

The right hand side of Equation 5 is composed of three terms, playing distinct roles in the inference process. $P(\tilde{\Delta h}|\Delta h, I)$ is called the *likelihood*. It represents the probability density of observing the glacier surface elevation changes as described by $\tilde{\Delta h}$ and a defined error model (see section 2.3.1) if we assume the true elevation map Δh and I to be known. This term captures all the uncertainties related to different topographic parameters (terrain roughness, elevation etc.) and cloud cover (see section 2.3.1).

$P(\Delta h|I)$ is called the *prior* and encodes all a priori information assumed about Δh, gathered from knowledge on the physics of glaciers and glacier dynamics. We discuss the prior term in greater details in section (see section 2.3.2).

Finally, $P(\tilde{\Delta h}|I)$ is a normalizing constant independent Δh and ensuring $\int P(\Delta h|\tilde{\Delta h}, I)d\Delta h = 1$. Its value is of no practical significance for this work. We shall thus neglect it and remember that the posterior PDF (Eq. 5) is defined up to a normalizing constant.

2.3.1 Likelihood: elevation data-related uncertainties

The first ingredient of Bayesian inference is the likelihood, which here captures the DEM-related errors by describing the probability of observing $\tilde{\Delta h}$ under a given an error model and prior information I: $P(\tilde{\Delta h}|\Delta h, I)$.

Terrain morphology and sample density have been documented as first-order controls of DEM accuracy and uncertainty (Aguilar et al., 2005; Wise, 2011; Mukherjee et al., 2013; Hubacek et al., 2016). When differencing stereo DEMs (ASTER for example), the DoD is likely to present aberrant $\tilde{\Delta h}$ values in areas with high terrain roughness such as steep rockwalls or clouded/low contrast zones, among others. Here, we use terrain roughness, hereafter denoted r, as the main descriptor for DEM errors and the main parameter for the error model.

Obscured regions in the input DEMs represent another major source of aberrant elevation change signal in DoDs (Paul, Bolch, et al., 2017), and will typically not dis-

play high roughness. Obscuring results from cloud cover or lack of contrast, mainly in DEMS processed from 8-Bit sensors (ALOS-PRISM, ASTER or, declassified KeyHole (KH) datasets such as Corona (KH4) or Hexagon (KH9), see Raup et al. (2015) for more) and is usually mitigated by masking obscured regions. In the present framework, we propose to capture obscuring within the likelihood and aim to evaluate how likely a specific $\tilde{\Delta h}_i$ is to result from obscured regions on DEM1 or DEM2. We typically expect aberrant elevation change signal to be either positive or negative, depending on whether the obscured regions are located on DEM1 or DEM2 and with greater absolute value than the geophysical signal. We however assume aberrant signal resulting from low-contrast area to be the same order of magnitude to that generated by the presence of clouds.

Given a pixel i, we consider three possible cases: either the pixel i of only DEM1 is obscured (event C_1), or pixel i of only DEM2 is obscured (event C_2), or the pixel is obscured in neither DEM (event C_0). We neglect the case where a same pixel is obscured on both DEMs at the same time. Marginalizing over all three cases, our likelihood writes as a mixture of conditional likelihoods:

$$\tilde{\Delta h}|\Delta h, I = \sum_{k=0,1,2} P(\tilde{\Delta h}|\Delta h, C_k, I)P(C_k|I) \tag{6}$$

The probabilities $P(C_1|I)$ and $P(C_2|I)$ are taken from the DEM's metadata (cloud cover extent provided by LPDACC for ASTER scenes for example) as well as the user's knowledge regarding each DEM's obscured extent, and we set $P(C_0|I) = 1-P(C_1|I)-P(C_2|I)$.

We first consider the conditional likelihoods for the simpler cases C_1 and C_2. Assuming the pixel i is obscured on DEM1 and not on DEM2 (case $C1$), then DEM1 measures $\tilde{h}_1 = z_{\text{cloud}}$ and therefore $\tilde{\Delta h} = \tilde{h}_2 - z_{\text{cloud}}$. With only prior information I, we assume $z_{\text{cloud}} \sim \text{Uniform}(z_{\text{SRTM}}(i), z_{\text{ceil}})$, where $z_{\text{SRTM}}(i)$ is the local ground elevation for pixel i read from an SRTM DEM (which is immune to cloud artifacts). z_{cloud} is a ceiling value for possible cloud altitudes, which we set to $z_{\text{cloud}} = 9000\,\text{m}$. Assuming that most of the error comes from DEM1 in this case and approximating $\tilde{h}_2 \approx h_2 \approx z_{\text{SRTM}}$, we find:

$$\tilde{\Delta h}|\Delta h, C_1, I \sim \text{Uniform}(z_{\text{SRTM}} - z_{\text{ceil}}, \Delta h). \tag{7}$$

Now assuming the pixel i is obscured on DEM2 and not on DEM1 (case $C2$), then DEM2 registers $\tilde{h}_2 = z_{\text{cloud}}$ and therefore $\tilde{\Delta h} = z_{\text{cloud}} - \tilde{h}_1$. With a similar reasoning to the C_1 case, we obtain:

$$\tilde{\Delta h}|\Delta h, C_2, I \sim \text{Uniform}(\Delta h, z_{\text{ceil}} - z_{\text{SRTM}}). \tag{8}$$

We now turn to the case when neither pixel is obscured (case C_0), in which we have to account for uncertainties caused by DEM errors. A typical approach to defining the likelihood would be to state that given any r one can expect $\tilde{\Delta h}$ to follow a Gaussian distribution centered on 0 (as we assume $\tilde{\Delta h} \neq 0$ is only due to the presence of geophysical signal) and with a standard deviation proportional to r (the higher r, the higher the statistical spread of the Gaussian distribution). This can however be a problematic in some cases, as Gaussian distributions are not robust to outliers. In this work, we prefer to follow the well-established practice of replacing Gaussian distributions with Student-t distributions, which present similar properties but feature heavier tails and are thus more robust to potential outliers. We therefore define our likelihood as following a Student-t distribution:

$$\tilde{\Delta h}|\Delta h, C_0, I \sim \text{Student}(0, g(r), k = 5) \tag{9}$$

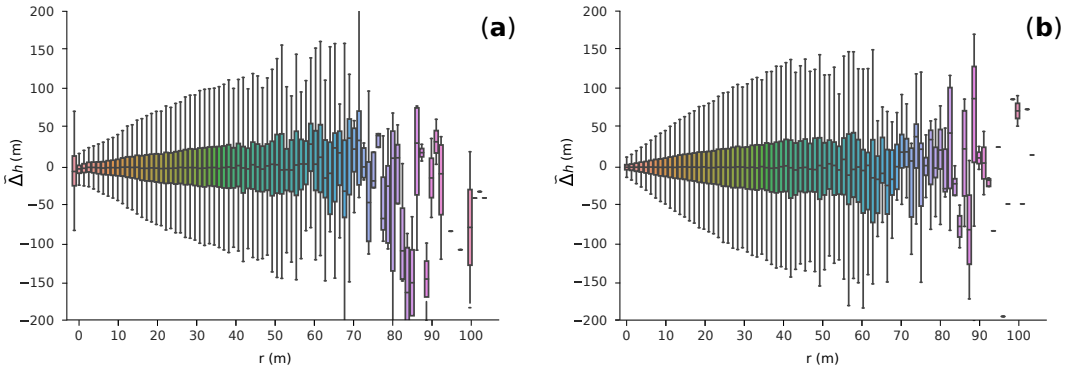

Figure 1: Distribution of $\tilde{\Delta h}$ per roughness bin. (a) computed from the difference between the SRTM C-Band DEM and ASTER DEMs (see Section 3 for more) over the Hunza Basin, Karakoram datasets. b) generated from $g(z)$ as fitted using data presented on panel a).

where $g(r)$ is a scale parameter controlling the statistical spread of the distribution and k is the number of degrees of freedom of the Student-t distribution. In practice, values of $3 \leq k \leq 10$ are recommended for inference problems (Gelman et al., 2013); we here use $k = 5$.

Considering that errors on Δh do not scale linearly with elevation (Holmes et al., 2000; Darnell et al., 2008), it is reasonable to assume similar non-linearity with roughness. We here use a data-driven approach to further describe the relationship between $\Delta\tilde{h}$ and r. Given a specific study zone (throughout the present example we use data from our first validation test case, see Section 3.1.1 for more), we first consider the computed $\Delta\tilde{h}$ DoD and a reference DEM from which roughness is computed. In practice we here use the SRTM C-Band DEM (see 3.2.1) and calculate terrain roughness using the Geospatial Data Abstraction Library (GDAL) roughness algorithm (largest inter-cell difference for a central pixel and it's surrounding cell see GDAL/OGR contributors (2021)). The histogram of $\Delta\tilde{h}$ per r bin gives further insight on $g(r)$ (Figure 1).

The spread of $\tilde{\Delta h}$ at low (i.e. relatively close to 0) roughness values on Figure 1 (a) is a consequence of the geophysical signal of glacier surface elevation change. The model $g(r)$ thus aims to replicate the spread of $\tilde{\Delta h}$ distributions for each r, as showed on Figure 1 (a). In the present case, we fit the generative model $g(r)$ to 1 standard deviation of the $\tilde{\Delta h}$ distribution per roughness bin. More formally, we thus define:

$$\mathrm{g(r)} = |\tanh\left(\frac{r}{s}\right)| * (\sigma_{r_max} - \sigma_{r_0}) + \sigma_{r_0} \tag{10}$$

where s is the resolution of the DEM used to compute the roughness, $\sigma_{\tilde{\Delta h}}(r_0)$ and $\sigma_{\tilde{\Delta h}} r_m ax$ are the standard deviations of the distribution $\tilde{\Delta h}$ for $r = 0$ and the maximum r value over the whole roughness map respectively. In practice, we find $\sigma_{\tilde{\Delta h}}(r_0) = 4$ m and $\sigma_{\tilde{\Delta h}} r_m ax = 30$ m to work best, and to be in the same order of magnitude as $\sigma_{\tilde{\Delta h}}$ values described by Gardelle et al. (2013). An example of $\sigma_{\tilde{\Delta h}}$ simulated using $g(r)$ is shown on Figure 1 B.

2.3.2 Priors: glacier dynamics

Now that we have detailed the likelihood $P(\tilde{\Delta h}|\Delta h, I)$, we turn to the description of the prior term in Eq. 5: $P(\Delta h|I)$.

The prior captures all information about Δh that is known regardless of $\tilde{\Delta h}$. In the present case, this comes from human expertise on glacier physics and previous measurements of glacier surface elevation changes in the studied contexts.

Surface elevation changes with altitude are mainly governed by the glacier's response to climate and the dynamics of glacier flow as these parameters have the most impact on the glacier's mass balance rate. Let us consider glacier-wide Δh for a glacier with negative mass budget. It is reasonable to assume that maximum reduction in surface elevation will occur at the tongue of the glacier. Following Schwitter and Raymond (1993), we can further assume than surface elevation lowering rates will non-linearly decrease with increasing altitude, possibly reaching positive Δh in the accumulation zone. The altitude, if it exists, at which $\Delta h \simeq 0$ is called the Equilibrium Line Altitude (ELA). This typical Δh pattern can however be strongly altered when studying surge-type glaciers, or glaciers presenting an substantial debris cover.

2.3.2.1 Surge-type glaciers Surge-type glaciers are characterized by a complex flow pattern, alternating between rapid unstable glacier flow (surge phase) and periods of stagnation or slow flow (quiescent phase) (Jiskoot, 2011; Benn et al., 2019; Truffer et al., 2021).

Surges initiate from an ice buildup in a reservoir zone, and propagate to a receiving zone, typically the glacier terminus. As a consequence of rapid downward mass transfer during surges, the glacier terminus usually advances and the glacier's surface elevation increases in the lowermost parts of the ablation zone (Rankl & Braun, 2016; Guillet et al., 2021).

Surging glaciers thus exhibit complex and contradictory Δh patterns. During the surge phase, surface elevation lowering in high altitude (in the reservoir zone, usually in the vicinity of the ELA) is associated to considerable surface elevation increase at comparatively low altitudes. During the quiescent phase a positive Δh signal is observed in high altitudes as the ice builds-up in the reservoir zone, while, in the ablation zone, the melting of stagnant or slow flowing ice leads to strongly negative Δh.

2.3.2.2 Debris-covered glaciers Supraglacial debris cover in the ablation zone will strongly influence the glacier's mass balance by directly affecting surface melt rates (Benn et al., 2012; Brun et al., 2018). A scattered, thin debris cover will typically lead to a local decrease in albedo, and thus, to an increase in melt rate while dense and thick debris covers usually provide insulation to the underlying ice Nakawo and Young (1981); Nicholson and Benn (2006); Pratap et al. (2015). Debris cover thus entails higher Δh variability in the ablation zone compared to what is usually observed for clean-ice glaciers (Brun et al., 2016).

We now come back to the formulation of our prior probability taking into account the above considerations. The aim here is to define, for each pixel of the DoD, a set of admissible Δh values considering glacier dynamics.

First, we define an elevation-dependent function to model glacier surface elevation variations:

$$\Delta_{h_i}(z_i) = e^{-\left(\frac{z_i - z_{\min}}{\mathcal{Z}}\right)} * (\delta_{h_{front}} - \delta_{h_{acc}}) + \delta_{h_{acc}} \tag{11}$$

with

$$\mathcal{Z} = \frac{z_{ELA} - z_{min}}{2} \tag{12}$$

where z_i is the elevation of i-th pixel on the elevation map, z_{min} is the minimum glacier elevation and z_{ELA} is the elevation of the equilibrium line. While z_{ELA} must be provided by the user and relies, for example, on previous publications from the same study zone, z_i and z_{min} are read directly from a DEM (SRTM-C DEM in the present cases, see Section 3 for more). $\Delta_{h_{front}}$ and $\Delta_{h_{acc}}$ respectively represent the maximum admissible accumulation at the terminus and in the accumulation zone of the glacier. For pixels at

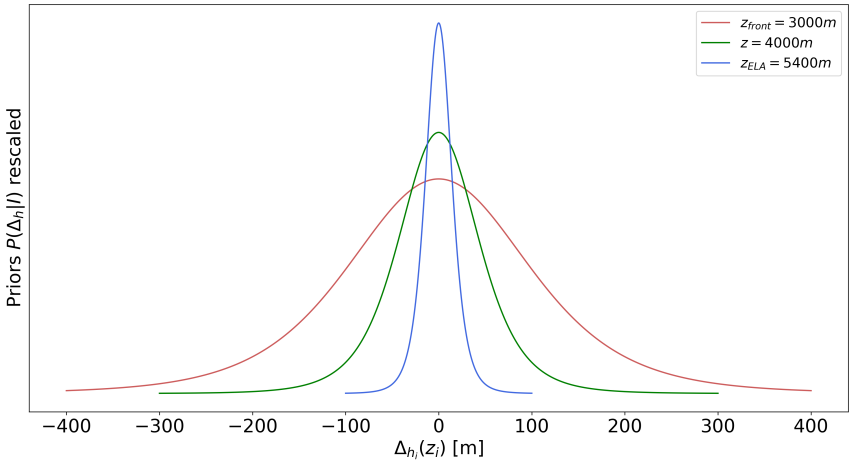

Figure 2: Example of prior distribution on Δh for a synthetic surge-type glacier spanning between 6000 and 3000 m a.s.l. of elevation. Priors are calculated at the front (red, 3000m a.s.l.) and the ELA (blue, 5400 m a.s.l.) of the glacier. The prior distribution at the front of the glacier (red) allows for both surging and rapid thinning related-extreme Δh values. Stricter priors at higher altitudes narrow admissible surface elevation changes.

higher elevations than the ELA, we define a stricter prior on Δh to rule out any unphysical surface elevation change. We formulate $|\delta_{h_{acc}}| = p{*}n_y$ where p captures the knowledge over the glacier's accumulation and n_y is the date range covered by the DoD. p can thus be the yearly mean precipitation in the study zone, or the direct accumulation rate derived from ice-core studies; both are typically derived from previous published results. Other mass gain process occurring in the accumulation zone such as avalanching and snow transportation by wind are not accounted for.

Similarly as in Section 2.3.1, we define $P(\Delta h|I)$ a Student-t distribution with $k = 5$ degrees of freedom and use $\Delta_{h_i}(z_i)$ as scaling parameter to control the statistical spread of the distribution:

$$\Delta h|I = \text{Student}(0, s, k = 5) \tag{13}$$

with:

$$s = \frac{\Delta_{h_i}(z_i)}{\delta_u} \tag{14}$$

where δ_u is the inverse cumulative distribution function of the Student-T distribution.

Figure 2 shows an example of priors for two pixels of a synthetic glacier extending from 6000 to 3000 m a.s.l. with chosen ELA of 5400 m. We defined the average yearly precipitation to be $0.5m * a^{-1}$ and $n_y = 10$. The weaker prior allows for greater variability in $\Delta_{h_i}(z_i)$ at the front of the glacier with values ranging between -300 and 300 (99% credible interval). Above the ELA, stricter constraints narrow the range of admissible $\Delta_{h_i}(z_i)$ values to [-40, 40](99% credible interval).

We have now specified the full prior (Equation 13, with terms discussed in Section 2.3.2) and likelihood using the error model (Equations 6, 9, 7, 8). We can therefore evaluate the posterior probability density using 5 for any value of $\Delta\tilde{h}$. The filtered value is finally computed by numerical integration as the median of the univariate posterior probability density function.

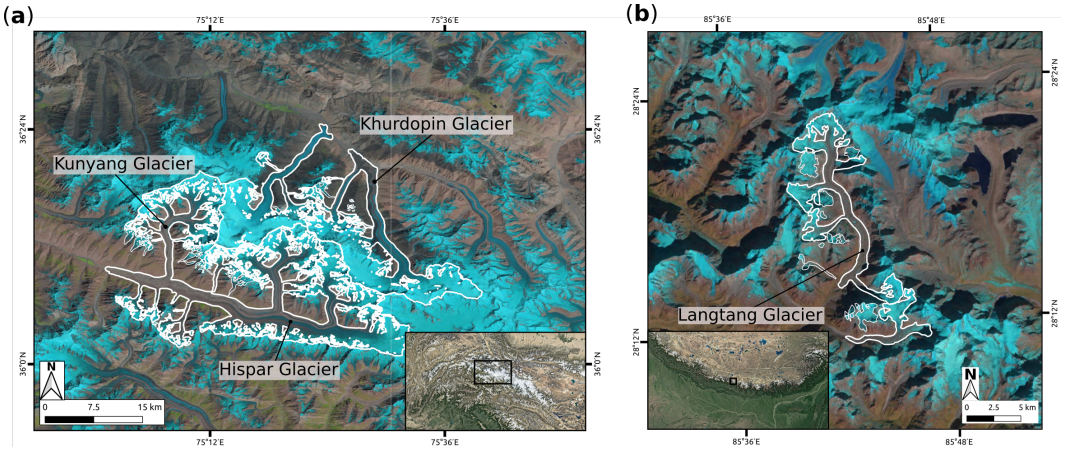

Figure 3: (a) : Location of Case Study 1 area in the Karakoram region (black square in Google Earth inset). The main investigated glaciers are represented by their outlines (white solid line) from the RGI V6.0. Baseline image is a natural color Landsat 8 OLI acquired on August 25 2020. b): Location of Case Study 2 area in the Central Himalaya (black square in Google Earth inset). The main investigated glaciers are represented by their outlines (white solid line) from the RGI V6.0. Baseline image is a natural color Landsat 8 OLI acquired on November 11 2020

3 Validation

In this section, we setup validation test cases to demonstrate the technique presented throughout the paper. Using a combination of DEMs of different origins (SRTM, ASTER, Hexagon KH-9 and Cartosat 1), we assess key aspects of our method, with an emphasis on surge-type and debris-covered glaciers. We consider the problem of estimating Δh from realizations of $\tilde{\Delta h}$ and knowledge on glacier physics, before comparing our DoDs with already published results.

3.1 Case studies areas

3.1.1 Case study 1 : Hispar and surrounding glaciers, Karakoram range, Pakistan

The Karakoram mountain range is widely known for its high abundance of surge-type glaciers. More specifically, glaciers in the Central Karakoram have been actively surging in the past 25 years. This intense surging activity yields complex surface elevation change patterns with a well-known co-existence of strong thinning and thickening rates, testifying for recent unstable glacier dynamics. Among the glaciers present in this case study, Hispar and Khurdopin glaciers (see Figure 3 a) recently (2015-17) displayed surge-type behavior (Paul, Strozzi, et al., 2017; Rashid et al., 2018; Guo et al., 2020).

In this validation case, we compare the surface elevation changes obtained by our method with the results of Bolch et al. (2017). We compute the 1999-2009 glacier surface elevation changes from the co-registered DEMs used in Bolch et al. (2017). We then illustrate goodness-of-fit by studying the residuals between the two DoDs. We first focus on glacier surface elevation changes over the whole study area, before emphasizing on the 2000-08 surge of Kunyang Glacier.

3.1.2 Case study 2 : Langtang Glacier, Central Himalaya, Nepal

Langtang Glacier is located in the eponymous valley in the central part of the Himalaya, approximately 70 km North of Kathmandu, Nepal. Ranging from 7119 to 4380 m a.s.l., Langtang Glacier displays an average slope of 18°(32%). Close to 35% of the glacier's area is covered with debris, most of them found in the ablation area below 5200 m a.s.l. (Figure 3 b)

In this validation case, we compare the surface elevation changes obtained by our method with the results published by Ragettli et al. (2016). Similarly to Case Study 1, we compute glacier elevation changes from co-registered DEMs generated by the authors and provided to us. Goodness-of-fit is then evaluated by studying the residuals between the generated DoD, and the one published by Ragettli et al. (2016), focusing on glacier-scale surface elevation differences.

3.2 Data

For both case studies we use DEMs that were provided to us by the authors. This allows us to cover DEMs generated from different acquisition protocols and instruments such as radar and satellite imagery. For any complementary information on the input datasets, we refer the reader to the specific publications.

3.2.1 SRTM

The Shuttle Radar Topography Mission (SRTM) was an 11-day mission carried out in February 2000 on board the space shuttle Endeavor. Near-global coverage was achieved between latitudes 56 °S to 60 °N (Farr et al., 2007). The C-band of the SRTM DEM presents a resolution of about 1 arc second ($\simeq$ 30 m grid) and is available via the U.S. Geological Survey (NASA, 2013). We here use the C-band SRTM DEM in two distinct steps. In the likelihood, the roughness map is computed from the C-band SRTM DEM. Similarly to D. Wang and Kääb (2015), we use the SRTM DEM as reference for the elevation-dependent surface elevation change law (Equation 11) in our prior.

3.2.2 ASTER

The 1999-2009 Hispar Glacier surface elevation changes (Case Study 1) originate from the difference of the C-Band SRTM DEM with various DEMs processed from images acquired by the Advanced Spaceborne Thermal Emission and Reflection Radiometer (ASTER)(Bolch et al., 2017). On-board the Terra satellite, ASTER creates clouds and land surface images from three different subsystems: the visible and near infrared (VNIR, 15 m resolution), the shortwave infrared (SWIR, 60 m resolution), and the thermal infrared (TIR, 90 m resolution). The 10 DEMs used by Bolch et al. (2017) are standard AST14DEM, computed using the SilcAst software from stereo-pairs acquired by the VNIR subsystem between 2008 and 2010.

3.2.3 Hexagon-KH9

Hexagon KeyHole-9 were a series of reconnaissance satellites operated between 1971 and 1986 at an altitude close to 171 km (Burnett, 2012). Images originating from the Hexagon KH-9 mission were declassified by the United States Geological Survey in 2002. The mapping camera system on-board Hexagon satellites (missions 1205-5 to 1216-5) acquired around 29000 images of 9 to 6 m of resolution on a global scale. In the present study, we do not generate digital elevation datasets from Hexagon-KH9 imagery and rather use the 1974 KH-9 DEM generated by Ragettli et al. (2016) (Case Study 2).

Case study 1: Hispar			Case Study 2: Langtang		
$\delta h_{front}[m]$	$\delta h_{acc}[m]$	z_{ELA}(m a.s.l.)	$\delta h_{front}/\delta t[m.a^{-1}]$	$\delta h_{acc}/\delta t[m.a^{-1}$	z_{ELA} (m a.s.l.)
200	4.5	5300	4	0.6	5400

Table 1: Summary of the priors used for the two case studies

3.2.4 Cartosat-1

The 1974-2006 Langtang Glacier surface elevation changes (Case Study 2) originate the difference of the KH-9 DEM with a DEM computed from a pair of images acquired by Cartosat-1 in November 2006. Cartosat-1 is a remote-sensing satellite developed and operated by the Indian Space Research Organization (ISRO) with a spatial resolution of 2.5 m (Ahmed et al., 2007). The DEM used in Ragettli et al. (2016) has been generated by the authors from radiometrically corrected along-track stereo imagery.

3.2.5 Glacier outlines

We used the openly available Randolph Glacier Inventory (RGI, version 6.0, Consortium et al. (2017)) glacier outlines to spatially constrain the computation of Δh estimates and for glacier-scale results visualization. As the terminus of Hispar (Case Study 1) and Langtang (Case Study 2) glaciers have shown limited changes over the past 120 years(Paul, Strozzi, et al., 2017; Wijngaard et al., 2019), we consider glaciers outlines to be constant over the studied intervals.

3.2.6 Priors

3.2.6.1 Case Study 1 - Hispar and Kunyang glaciers The parameters used to compute the prior probability in Case study 1 are summarized in Table 1.

While the considered period is rather short, previous surge events in the Karakoram have shown large magnitudes (Quincey & Luckman, 2014). We typically constrain $|\Delta_{h_{front}}| \leq 300m$ for altitudes under the glacier's equilibrium line as it is the higher-end of the spectrum of surging-induced surface elevation changes (Cuffey & Paterson, 2010). For δh_{acc}, we follow D. Wang and Kääb (2015) and define the maximum accumulation cannot exceed the average precipitation over the considered time period. Here we used a yearly mean precipitation of $0.5m.a^{-1}$ as estimated by Immerzeel et al. (2012). Finally, we take $z_{ELA} = 5300$ m a.s.l., as defined by Mukhopadhyay and Khan (2016), and assume it constant over the 1999-2008 time period as the glaciers exhibited balanced mass budgets in this region during the last decades (Gardelle et al., 2013; Bolch et al., 2017).

3.2.6.2 Case Study 2 - Langtang and surrounding glaciers Similarly to Case Study 1, the parameters used to compute the prior probability in Case study 2 are summarized in Table 1.

As no surges have been documented in the Langtang basin, we use a narrower prior for frontal elevation changes. Based on modeled and remotely sensed Δh in the study region, we consider $|\delta h_{front}| = 4m.a^{-1}$ to be admissible (Wijngaard et al., 2019). We stress that, while mass gain at the front of a non-surge type glacier is unphysical, this value captures the spread of the distribution of admissible Δh at the front of the glacier

and thus affects similar probabilities to positive and negative values. Ice cores studies in the Langtang region have documented accumulation rates close to $\delta h_{acc} = 0.6m.a^{-1}$. Finally, we take $z_{ELA} = 5400$ m a.s.l., as defined by Ragettli et al. (2016), and assume it constant over the 1974-2006 time period.

3.3 Surface elevation changes validation

In the following sections, surface elevation change DEMs represent the best Δh estimate computed by their respective authors. Regardless of the method used to computed them, these surface elevation change datasets will be labeled Δ_{hXXX}, where XXX is a dataset-specific suffix. For DoDs generated in the present study, XXX indicates the represented quantile of the posterior probability distribution on Δh; Δh_{50} is, for example, the DoD of the median surface elevation change.

For the sake of clarity and readability, the presented DoDs are neither reprojected nor presented onto any basemap or other digital elevation dataset.

3.3.1 The surge of Kunyang Glacier : 2000-2008

We here present surface elevation changes as different DoDs, shown in Figure 4. The first DoD is formed from the median of the posterior probability distribution for each pixel, while subsequent DEMs represent the associated 68 and 90% credible intervals respectively. The accumulation zones of the studied glaciers appear to be regions of high uncertainty, with the 90% CI of pixel distributions reaching close to 75m. The broader posterior on Δ_h in the higher altitudes regions is due to a combination of effects : the increased roughness in high-relief north faces, the presence of clouds and lower contrast on the ASTER DEM.

We further compare our results to the 1999-2009 DEM published in Bolch et al. (2017) (Δh_{B17}) in Figure 5. We find that Δh_{50} and Δh_{B17} are in good agreement throughout the study area. From the map of residuals (Figure 5), we see that both the surge of Kunyang Glacier (the westernmost tributary of Hispar Glacier, Figure 3 a) and Khurodpin Glacier's heavily contrasted Δh signal are particularly well represented, with similar orders of magnitude. Noticeable differences can however be observed, mainly in the accumulation zone of Kunyang Glacier. The Δh_{B17} DoD indeed presents pixels indicating extreme accumulation values (up to 154 m of elevation gain) along the ridge between Trivor Sar (7577 m a.s.l) and Disteghil Sar (7885 m a.s.l.). Similarly, we observe strong mass gain (up to 147m) in the nearby accumulation zones of the western and eastern branches of Kunyang Glacier. Such mass gain being very unlikely given the site topography, we believe these accumulation values to be the consequence of low contrast and clouds on the ASTER DEM. These outliers appear to have been filtered on Δh_{50} , where highest estimated mass gain is around 30 m.

Over the whole study area, the distributions of pixel values are very similar Δh_{B17} and Δh_{50} (Figure 6). Both display heavy tails and are non-Gaussian. The two distributions however present sensitively different medians (Δh_{B17} : 0.0 m, Δh_{50} : 2.7 m) and Inter-Quartile Range (IQR, Δh_{B17} : 7 m, Δh_{50} : 13 m). While we observe a mainly linear relationship of equation $y = x$ between the pixel values of the different DoDs, we further note the presence of an important cluster of 0-valued pixels in Δh_{B17} , altering the linear relationship between the two DoDs for values ranging from -100 m to around 150 m (Figure 7). Zero-valued pixels in Δh_{B17} mainly appear at high altitude, in the accumulation zone of the studied glaciers (Figure 8) and correspond to regions of highest uncertainty in Figure 4. We here interpret such a prominent clustering as an artifact generated by the filtering and gap filling method used by the authors. Bolch et al. (2017) indeed used the method described in Pieczonka and Bolch (2015) (see section 2.2.1) to filter outliers and OK to fill data voids in the DoD.

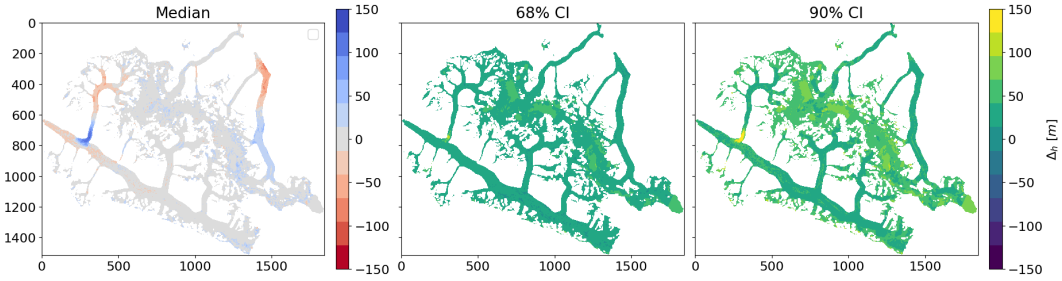

Figure 4: Δh_{B17} (left) and Δh_{50} (right). Bottom represents the residuals computed by subtracting Δh_{B17} and Δh_{50} . Note the overall similarity in the two DoDs computed with different methods.

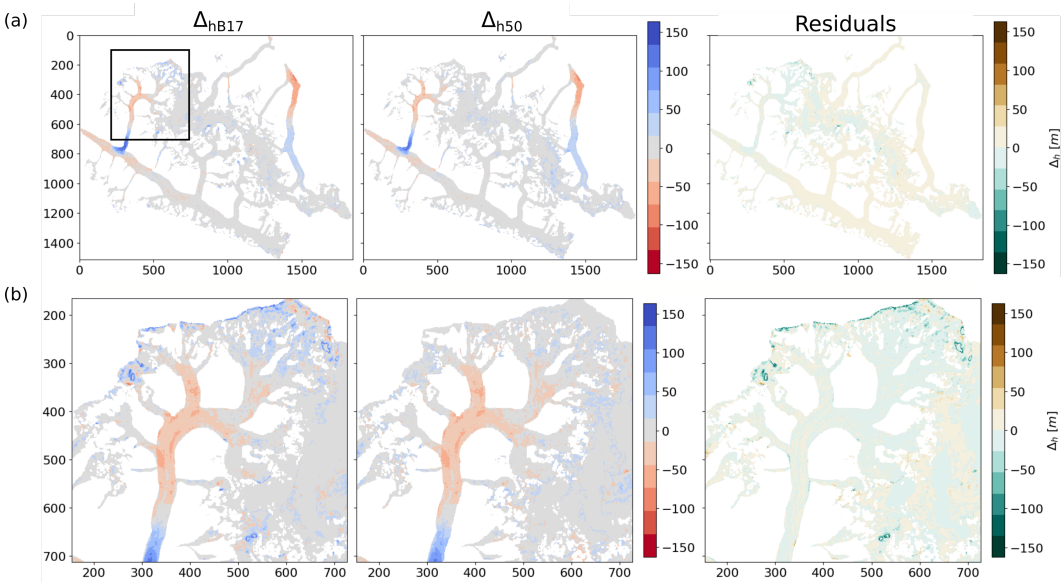

Figure 5: Comparison between Δh_{B17} (left) and Δh_{50} (center), with plotted residuals obtained by differencing Δh_{B17} and Δh_{50} (right). (a) covers Hispar, Kunyang, and Khurdopin glaciers in their entirety. (b) is a closeup of the accumulation zone of Kunyang Glacier. Non-filtered outliers are clearly visible, resulting from poorly contrasted terrain.

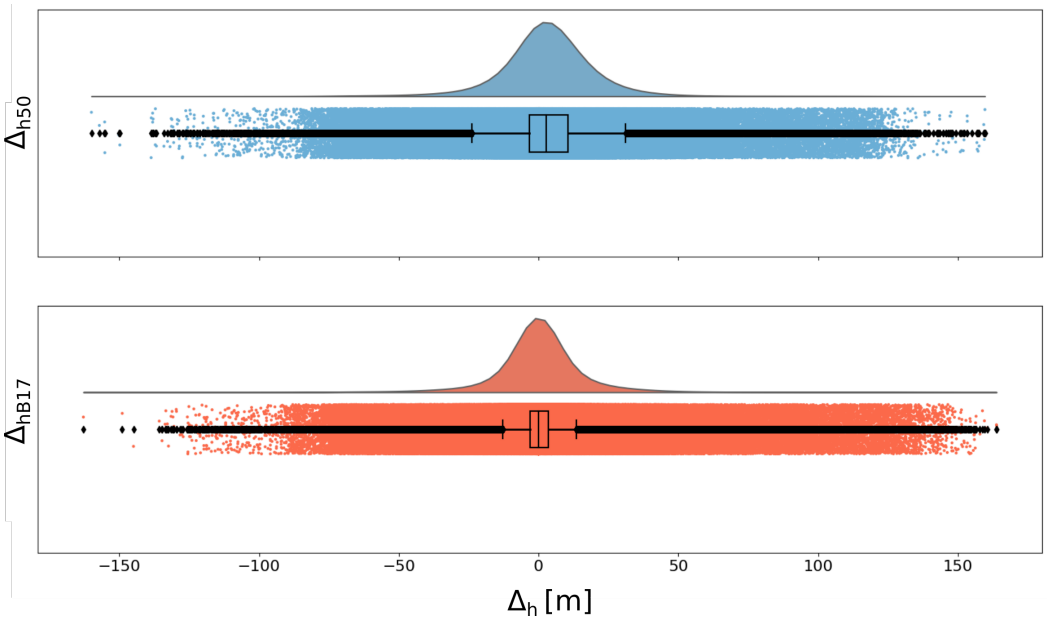

Figure 6: Distribution of raster values for the two Case study 1 glaciers DoDs.

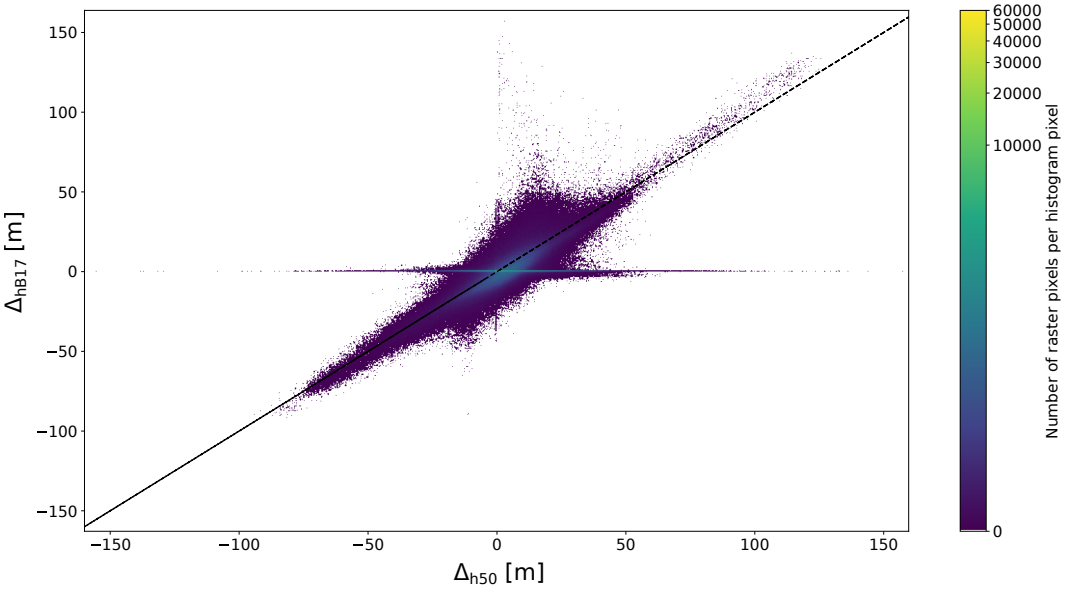

Figure 7: Bivariate scatter density histogram of the relationship between Δh_{B17} and Δh_{50} . Note the substantial cluster of O-valued pixels in Δh_{B17} . Dashed line represents $y = x$.

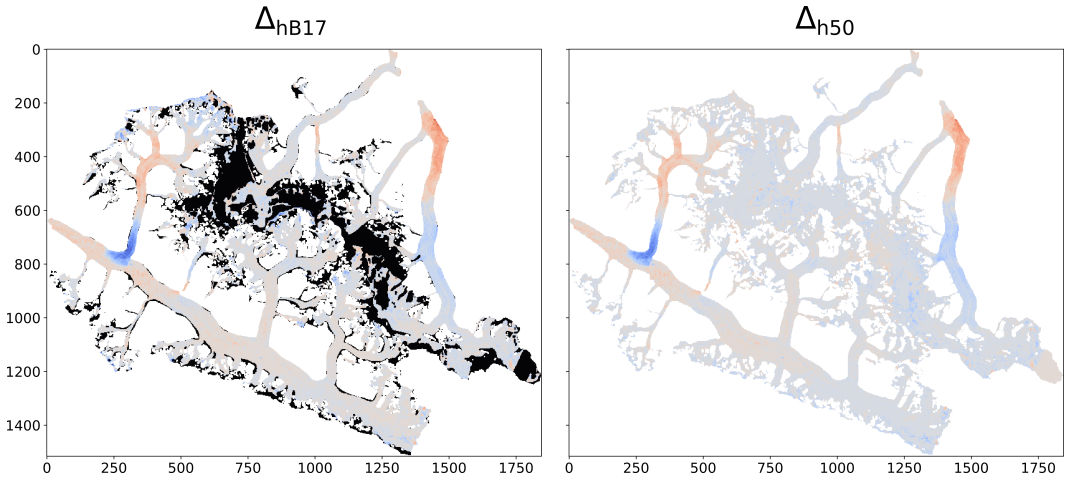

Figure 8: Comparison between Δh_{B17} and Δh_{50} , similar to Figure 5. Pixel with values of 0.00 are represented in black on both DoDs. 10% of Δh_{B17} is covered with artificial zero-valued pixels.

3.3.2 Langtang and surrounding glaciers : 1974-2006

Accumulation zones appear to be regions of high uncertainty with the 90% credible interval reaching 2 $m.a^{-1}$ (Figure 9). Highly uncertain Δh estimates are mainly clustered in the accumulation zone of Langtang Glacier and its tributaries. These are the direct consequence of obscured regions on the Cartosat-1 image affecting the DEM. We finally note that the overall uncertainty on $\Delta h/\Delta t$ increases in regions of the ablation zone displaying higher ice cliffs concentration (Ragettli et al., 2016), as a result of our error model formulation.

Similarly to Case Study 1, we find that the two DoDs are in good agreement (Figure 10). Values in Δh_{R16} reach $+0.5m.a^{-1}$, with extrema close to $+4.0m.a^{-1}$ in the accumulation zone of the southernmost tributary of Langtang Glacier. At similar locations in Δh_{50} , Δ_h estimates are typically close to $+0.2m.a^{-1}$ with extreme values reaching $+2.3m.a^{-1}$ (Figure 10). The distributions of raster values are consistent, with similar medians (Δh_{50} : $-0.31m.a^{-1}$, Δh_{R16} : $-0.27m.a^{-1}$) and IQR (Δh_{50} : $0.59m.a^{-1}$, Δh_{R16} : $0.62m.a^{-1}$) (Figure 11). The distribution of raster values for Δh_{50} however does not display as heavy tails as that of Δh_{R16} . This can be explained by the use of stricter priors for this particular case study, resulting in more pixel values being classified as outliers.

The scatter density histogram (Figure 12) shows identical patterns to those identified in Case Study 1, with clustering of near-0 values on Δh_{R16} . We here observe distinct clusters of values between 0.0 and -0.2, spanning over the entire raster value space in Δh_{50} . Figure 12 further highlights a minor cluster of 0-valued pixels in Δh_{50} . While we interpret the latter to be an artifact of the polygon clipping algorithm (Figure 13) (Sutherland & Hodgman, 1974; Horowitz & Papa, 1992), the former likely result from the gap filling method used in Ragettli et al. (2016). Figure 13 indeed highlights that artificial clusters of near-0 valued pixels primarily appear in high uncertainty regions in the accumulation zone (obscured by clouds on Cartosat-1), with scarce occurrences in the ablation zone of Langtang Glacier (high ice cliff concentration). Finally, patterns generated by the elevation-band gap filling methodology used in Ragettli et al. (2016) are clearly identifiable on the western tributaries of Langtang Glacier (Figure 13, x : $[0, 100]$, y : $[200, 300]$).

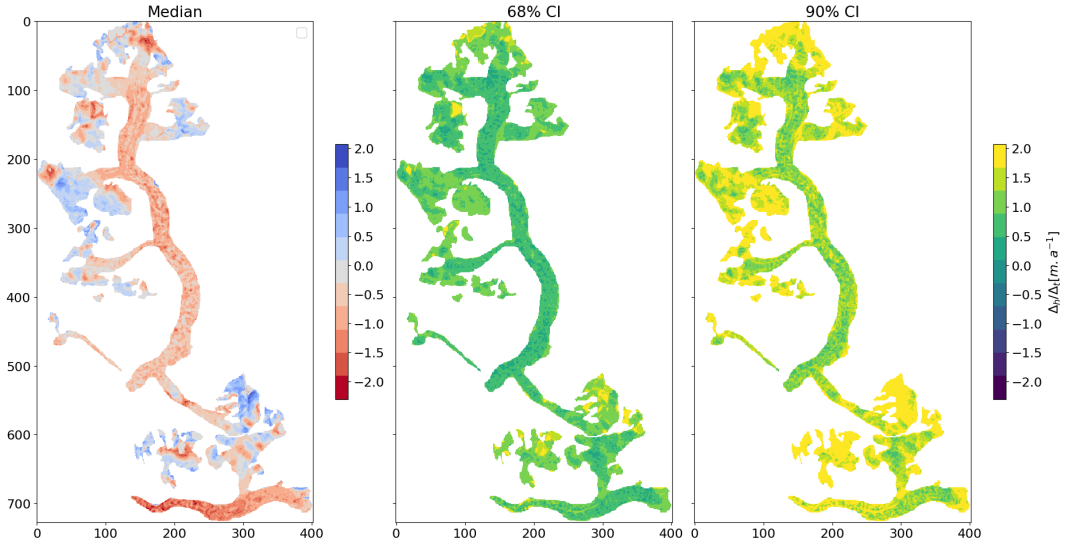

Figure 9: Δh_{50} for the Langtang case study and the associated credible region Δh_{68} and Δh_{90} . Note that the zones of higher uncertainty on glacier tongues are zones with the highest percentage of ice cliffs. Yellow zones in the accumulation zones on Δh_{68} result from obscuring on the Cartosat-1 image affecting the DEM.

4 Discussion

4.1 Probabilistic formulation of DEM differencing and Δh estimates

In Section 3, we designed two case studies to compare our Δh estimates to that of already published studies. In both cases, the DEMs produced with the proposed methodologies appeared consistent with the validation datasets and are accurate to the level of our input data. We however highlighted the existence of clusters of 0 or near-0 valued pixels in both case studies (Δh_{B17} and Δh_{R16}). We further argue that these clusters are artifacts resulting from the outlier filtering and linear interpolation methodologies used in Ragettli et al. (2016) and Bolch et al. (2017). The developed method allows to avoid artificial clustering of anomalous values by unifying outlier filtering and gap filling within a statistically coherent framework. Formulating the DEM differentiation as a Bayesian inference problem together with probabilistic uncertainty models further allows quantify and propagate associated uncertainties.

We finally demonstrated that none of the studied glacier surface elevation change distribution is Gaussian. Yet, glacier surface elevation change estimates are often reported in the literature as a mean and the associated standard deviation. While the assumption of normally distributed surface elevation changes might hold at global scales (Central Limit Theorem), our study shows that regional glacier thickness variations commonly follow skewed or heavy-tailed distribution, especially in contexts of dynamic instabilities or extensive debris cover (Kargel et al., 2014; Nilsson et al., 2015; Guillet et al., 2021). We here recommend to report further glacier surface elevation changes as a median associated to confidence intervals (as done here or in Dehecq et al. (2020) for example), typically a 68 and 90% CI. By doing so, one indeed provides the community with a quantification of the uncertainty associated with the elevation change over the whole glacier. Furthermore, the use of two credible intervals conveys a clearer view of the potential skewness, tails, and overall shape of the surface elevation changes distribution. Global error metrics cannot however capture the heteroskedastic behavior of the uncertainty associ-

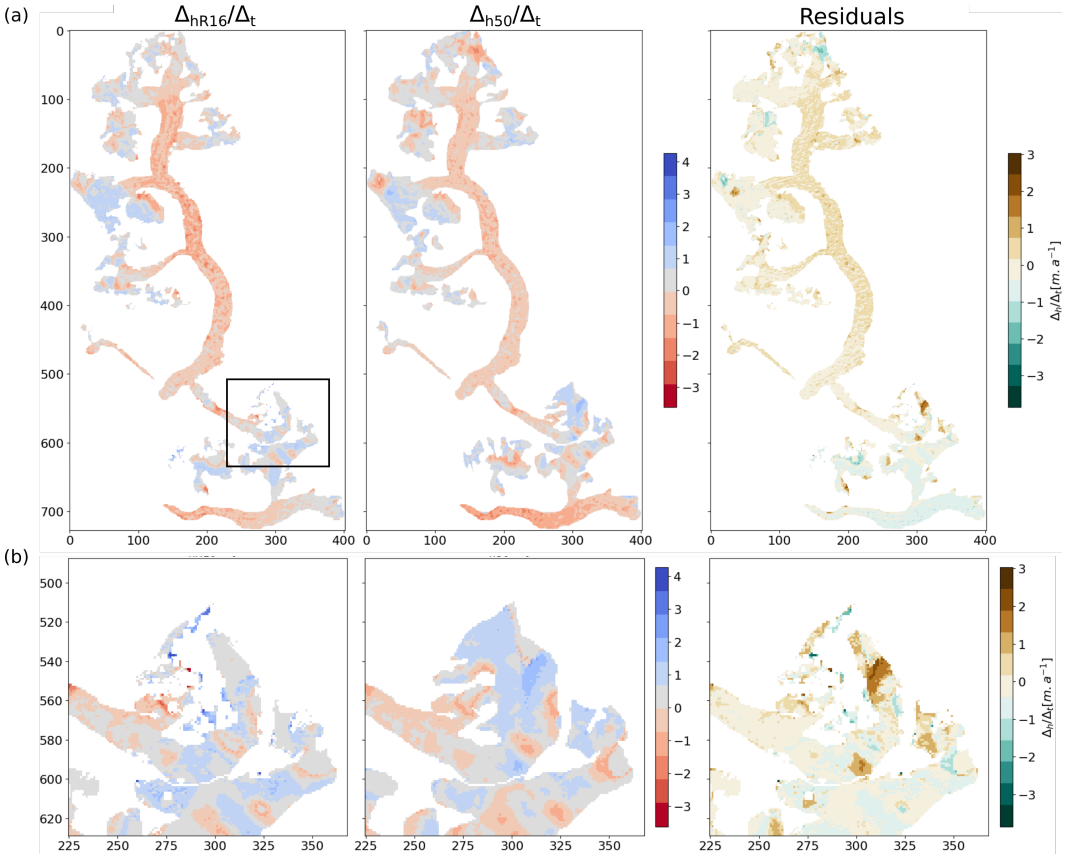

Figure 10: Comparison between Δh_{R16} (left) and Δh_{50} (center), with plotted residuals obtained by differencing Δh_{R16} and Δh_{50} (right). (a) covers Langtang Glaciers in their entirety. (b) is a closeup of the accumulation zone of a tributary of Langtang Glacier. Non-filtered outliers are clearly visible and data gaps are clearly visible on Δh_{R16} , resulting from poorly contrasted terrain.

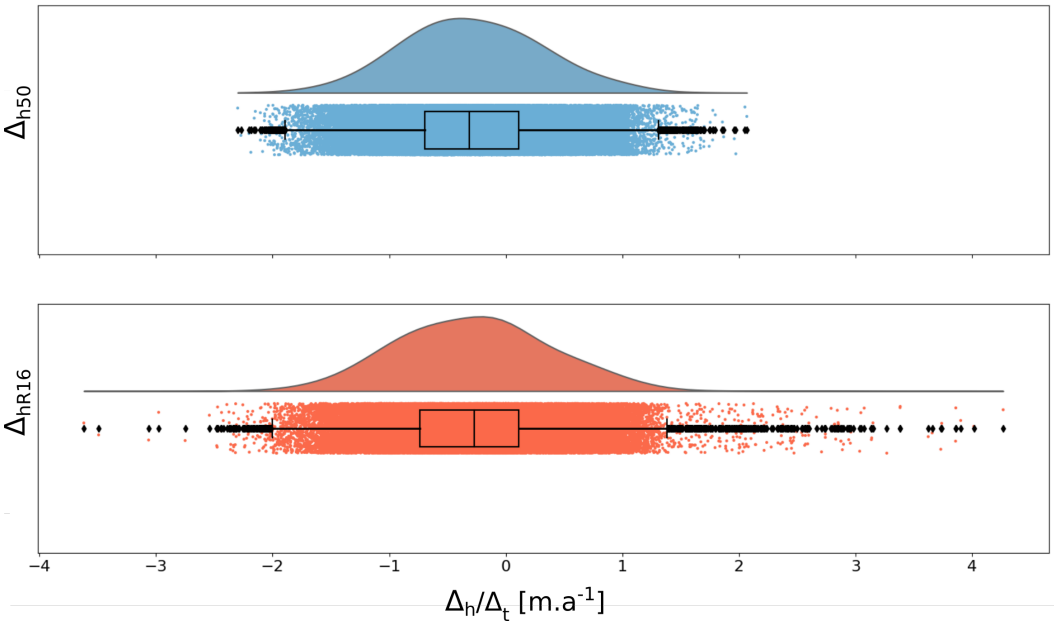

Figure 11: Distribution of raster values for the two Langtang Glacier DoDs.

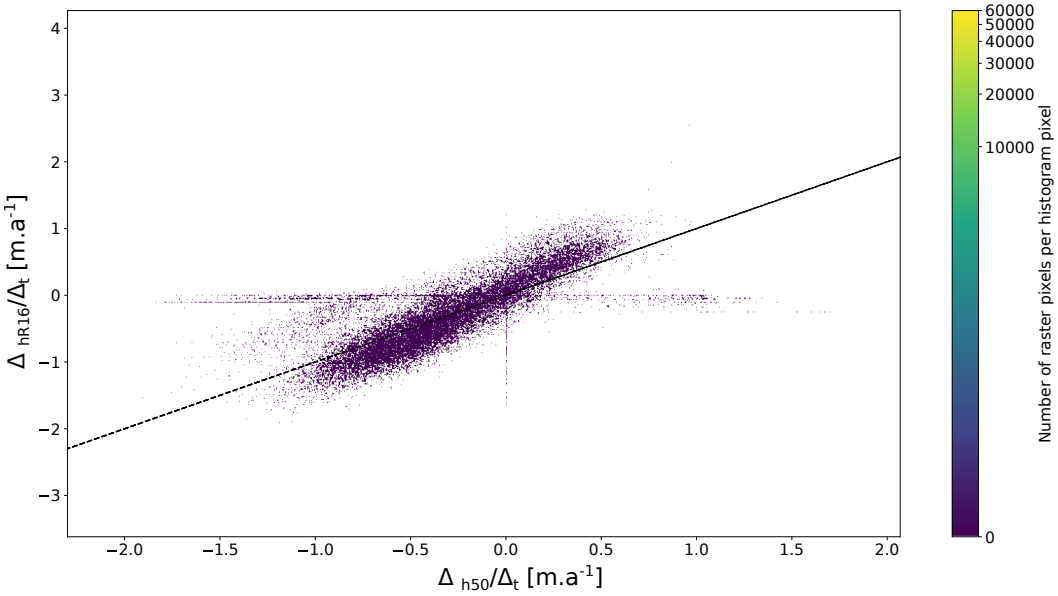

Figure 12: Bivariate scatter density histogram of the relationship between Δh_{R16} and Δh_{50} . Note the different cluster of near-0 valued p ixels in Δh_{R16} . A similar cluster of 0-valued pixels can be observed in Δh_{50} .

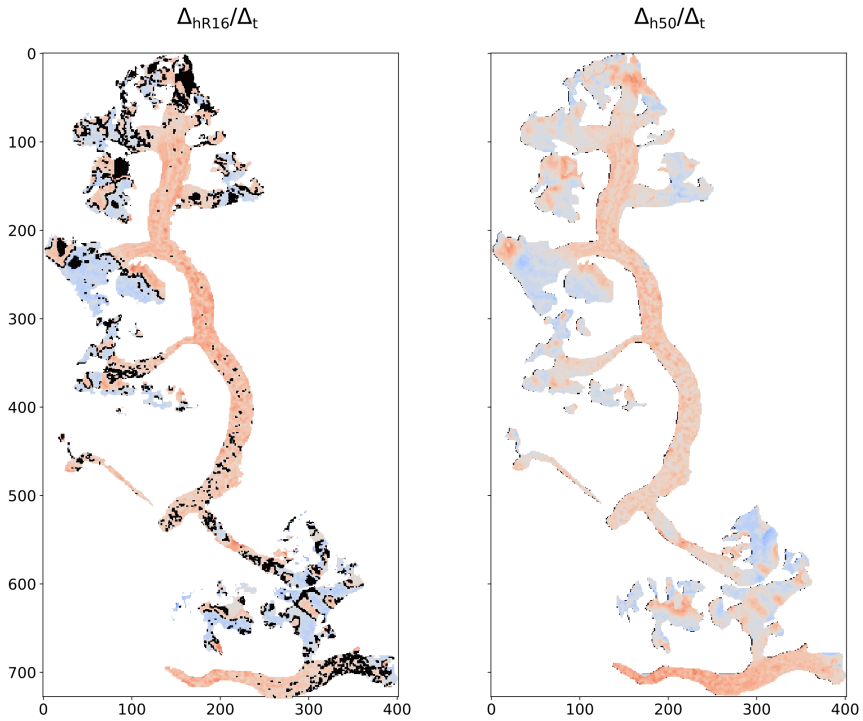

Figure 13: Comparison between Δh_{R16} and Δh_{50} . The data presented is the same as as Figure 10. Pixels with value within the $[-0.2, -0.045]$ interval are represented in black on Δh_{R16} . 0-valued pixels are similarly represented on Δh_{50} .

ated to surface elevation change estimates. While less practical than global error metrics, uncertainty maps like presented here appear to be the most accurate way of representing the level of certainty available over the proposed glacier surface elevation change estimates.

4.2 The use of the median of the posterior distribution in Bayesian inference

In the present paper, we decided to describe the posterior distribution on Δh using the median and the 90% credible interval. Another estimator commonly used in Bayesian inference problems is the Maximum A Posteriori (MAP) which corresponds to the mode of the posterior distribution. While no estimator can be defined as superior to the other, we have chosen to use the median and the associated credible interval for several reasons (Gelman et al., 2013, 2020). First, the MAP is a point estimate. Providing a single point estimate of the unknown quantity is not representative of Bayesian methods, which use distributions to infer unknown quantities from data. Second, the posterior probability density is multi-modal. Identifying the highest mode can thus be impossible as, in some cases, the different modes are equal (Lehmann & Casella, 2006; Casella & Berger, 2021). Finally, even if the highest mode can be identified, it is unlikely representative of the posterior distribution. While the mean of the posterior probability density is not always the most probable value, it allows, alongside the credible interval, to better characterize the posterior PDF in its entirety and thus provide a clearer picture of the uncertainty associated to each surface elevation change estimate.

4.3 Spatial correlation of DEM uncertainties

The present method is based on a probabilistic modeling of elevation data uncertainties, where terrain roughness is used as the main uncertainty descriptor. By computing glacier surface elevation differences pixel by pixel, we implicitly assume that neighboring pixels are independent and that uncertainties are uncorrelated. Many authors have however demonstrated, modeled and discussed the heteroskedastic behavior of uncertainties in elevation data (Monckton, 1994; Kyriakidis et al., 1999; Bretherton et al., 1999; Liu & Jezek, 1999; Wechsler & Kroll, 2006; Dehecq et al., 2020).

Following Hunter and Goodchild (1997), Guillet et al. (2020) proposed a method for modeling heteroskedasticity in DEM uncertainties within a probabilistic framework. They showed that correlated discrete random DEM perturbations can be generated from a Gaussian random field with a well-defined autocorrelation scale. The computational load of this operation is however prohibitive for large scale applications. Considering a $N*M$ pixels DEM, the method proposed by Guillet et al. (2020) requires inverting a covariance matrix of size $(N*M)*(N*M)$. Inverting such a matrix is a quadratically time-complex operation that cannot be done efficiently by general algorithms and requires problem-specific solutions (Sang & Huang, 2012; Zhang et al., 2018) such as covariance localization (see Hamill et al. (2001) and Ruggiero et al. (2016) for example).

The aim of the method proposed here is to be used for both glacier- and region-wide production of DoDs while maintaining a reasonable computing time. Numerical simulations have shown that, while often seen as a worst-case-scenario, assuming uncorrelated DEM error does not generate maximum variability in DEM derivatives (Oksanen & Sarjakoski, 2005; Dehecq et al., 2020). We thus argue that not accounting for heteroskedasticity in DEM error is unlikely to alter the presented results significantly enough, while requesting prohibitive computational time and power. Spatial correlation of DEM error however remains an important source of uncertainty in DEM-based geoscientific analyzes (see Dehecq et al. (2020) for more) and further work is thus needed to find an adequate formulation of this problem within probabilistic frameworks.

4.4 Physics-based probabilistic framework

In this paper, we have presented a method aiming to unify simple glacier elevation change and uncertainty modeling within a statistically consistent framework. The glacier surface elevation change model however relies on knowledge of the ELA. The equilibrium line altitude is defined up to a certain level of certainty and varies over annual and multi-decadal time scales. The uncertainty over the ELA itself depends on the estimation methods (see Braithwaite and Raper (2009) or Pandey et al. (2013) for example). We thus tested the impact of ± 150 m variations in the ELA for each case study (data not shown) and did not observe significant changes in the computed glacier surface elevation change estimates.

While the present methods focused on glacier surface elevation changes, it can be extended to other remotely-sensed glacier observations such as surface velocity or gravitational field for example. The models depicted in the present paper are very general and can be extended to other types of measurements and uncertainties, provided that they can be modeled satisfactorily (See Altena and Kääb (2017); Altena et al. (2021) for example).

4.5 Towards a fully probabilistic formulation of the geodetic mass balance

From Δh results, one can easily compute the total volume change (Δ_V) by integrating $\tilde{\Delta h}$ over the entire grid considered in the study area. Δ_V (or sometimes the rate of volume change, $\dot{V}$) is then used to compute the total mass change Δ_M (rate of mass

change, $\dot{M}$). Volume is converted to mass using a constant mass conversion factor ($f_{\Delta_V} = 850 \pm 60 kgm^{-3}$) defined by Sapiano et al. (1998) and Huss (2013).

Huss (2013) however demonstrated the high variability of f_{Δ_V} as well as the shortcomings of assuming a constant mass conversion factor. The $f_{\Delta_V} = 850 \pm 60 kgm^{-3}$ approximation is described as conditional on heavy assumptions (study period longer than five years, stable mass balance gradients, presence of firn area and $\Delta_V \neq 0$) and is likely to be a predominant, yet underestimated, source of uncertainty in geodetic mass balances. Given the widespread use of glacier geodetic mass balance as input in, for example, hydrological and runoff models, we want to restate the necessity of better uncertainty quantification in geodetically determined glacier mass balance.

A logical continuation of the method presented here is be to propose a probabilistic formulation of f_{Δ_V}. Introducing a spatially variable model for f_{Δ_V}, similarly to our prior (Section 2.3.2), and expressing it as a probability distribution rather than a single value estimate would indeed lead to further constrain the uncertainty associated to f_{Δ_V}.

5 Conclusions

In this paper, we presented a novel method for estimating glacier surface elevation changes from different DEMs. Driven by the goal of characterizing uncertainties on the surface elevation variations generated from DEM differentiation, we introduced models for admissible surface elevation change based on glacier physics as well as for characterizing uncertainties in co-registered digital elevation models. We integrated these ingredients into a statistically coherent Bayesian framework, which can readily be extended to other remotely-sensed glacier observations. We applied and validated the method for outlier filtering and void filling, before estimating glacier surface elevation variations. Our method produced surface elevation DoDs which are consistent with previously published results, while avoiding caveats such as artificial clustering of aberrant values. Combining Bayesian outlier filtering and gap filling with probabilistic uncertainty models, the method consistently estimates surface elevation variation for different glacial contexts, while also propagating the associated uncertainties. Applied to our particular problem, our study showed the potential importance of accounting for unstable and non-standard glacier dynamics, as it can otherwise result in significant biases.

References

Aguilar, F. J., Agüera, F., Aguilar, M. A., & Carvajal, F. (2005, July). Effects of Terrain Morphology, Sampling Density, and Interpolation Methods on Grid DEM Accuracy. *Photogrammetric Engineering & Remote Sensing*, *71*(7), 805–816. doi: 10.14358/PERS.71.7.805

Ahmed, N., Mahtab, A., Agrawal, R., Jayaprasad, P., Pathan, S. K., Ajai, ... Singh, A. K. (2007, June). Extraction and validation of cartosat-1 DEM. *Journal of the Indian Society of Remote Sensing*, *35*(2), 121. doi: 10.1007/BF02990776

Aizen, V. B., Kuzmichenok, V. A., Surazakov, A. B., & Aizen, E. M. (2006). Glacier changes in the central and northern Tien Shan during the last 140 years based on surface and remote-sensing data. *Annals of Glaciology*, *43*, 202–213. doi: 10.3189/172756406781812465

Altena, B., & Kääb, A. (2017, March). Elevation Change and Improved Velocity Retrieval Using Orthorectified Optical Satellite Data from Different Orbits. *Remote Sensing*, *9*(3), 300. doi: 10.3390/rs9030300

Altena, B., Kääb, A., & Wouters, B. (2021, September). *Correlation dispersion as a measure to better estimate uncertainty of remotely sensed glacier displacements* (Preprint). Glaciers/Remote Sensing. doi: 10.5194/tc-2021-202

Benn, D. I., Bolch, T., Hands, K., Gulley, J., Luckman, A., Nicholson, L. I., ... Wiseman, S. (2012, August). Response of debris-covered glaciers in the Mount Everest region to recent warming, and implications for outburst flood hazards. *Earth-Science Reviews*, *114*(1), 156–174. doi: 10.1016/j.earscirev.2012.03.008

Benn, D. I., Fowler, A. C., Hewitt, I., & Sevestre, H. (2019, October). A general theory of glacier surges. *Journal of Glaciology*, *65*(253), 701–716. doi: 10.1017/jog.2019.62

Beyer, R. A., Alexandrov, O., & McMichael, S. (2018). The Ames Stereo Pipeline: NASA's Open Source Software for Deriving and Processing Terrain Data. *Earth and Space Science*, *5*(9), 537–548. doi: 10.1029/2018EA000409

Bhambri, R., Hewitt, K., Kawishwar, P., & Pratap, B. (2017, November). Surge-type and surge-modified glaciers in the Karakoram. *Scientific Reports*, *7*(1), 15391. doi: 10.1038/s41598-017-15473-8

Bhattacharya, A., Bolch, T., Mukherjee, K., King, O., Menounos, B., Kapitsa, V., ... Yao, T. (2021, July). High Mountain Asian glacier response to climate revealed by multi-temporal satellite observations since the 1960s. *Nature Communications*, *12*(1), 4133. doi: 10.1038/s41467-021-24180-y

Bhushan, S., Shean, D., Alexandrov, O., & Henderson, S. (2021, March). Automated digital elevation model (DEM) generation from very-high-resolution Planet SkySat triplet stereo and video imagery. *ISPRS Journal of Photogrammetry and Remote Sensing*, *173*, 151–165. doi: 10.1016/j.isprsjprs.2020.12.012

Bingham, A. W., & Rees, W. G. (1999, January). Construction of a high-resolution DEM of an Arctic ice cap using shape-from-shading. *International Journal of Remote Sensing*, *20*(15-16), 3231–3242. doi: 10.1080/014311699211723

Bolch, T., Buchroithner, M., Pieczonka, T., & Kunert, A. (2008). Planimetric and volumetric glacier changes in the Khumbu Himal, Nepal, since 1962 using Corona, Landsat TM and ASTER data. *Journal of Glaciology*, *54*(187), 592–600. doi: 10.3189/002214308786570782

Bolch, T., Kamp, U., & Olsenholler, J. (2005). Using ASTER and SRTM DEMs for studying geomorphology and glaciation in high mountain areas. In M. Oluić (Ed.), *Bolch, Tobias; Kamp, Ulrich; Olsenholler, Jeffrey (2005). Using ASTER and SRTM DEMs for studying geomorphology and glaciation in high mountain areas. In: Oluić, Marinko. New Strategies for European Remote Sensing. Rotterdam: Millpress, 119-127.* (pp. 119–127). Rotterdam: Millpress. doi: 10.5167/uzh-137249

Bolch, T., Pieczonka, T., & Benn, D. I. (2011, April). Multi-decadal mass loss of glaciers in the Everest area (Nepal Himalaya) derived from stereo imagery. *The Cryosphere*, *5*(2), 349–358. doi: 10.5194/tc-5-349-2011

Bolch, T., Pieczonka, T., Mukherjee, K., & Shea, J. (2017, February). Brief communication: Glaciers in the Hunza catchment (Karakoram) have been nearly in balance since the 1970s. *The Cryosphere*, *11*(1), 531–539. doi: 10.5194/tc-11-531-2017

Braithwaite, R. J., & Raper, S. C. B. (2009). Estimating equilibrium-line altitude (ELA) from glacier inventory data. *Annals of Glaciology*, *50*(53), 127–132. doi: 10.3189/172756410790595930

Bretherton, C. S., Widmann, M., Dymnikov, V. P., Wallace, J. M., & Bladé, I. (1999, July). The Effective Number of Spatial Degrees of Freedom of a Time-Varying Field. *Journal of Climate*, *12*(7), 1990–2009. doi: 10.1175/1520-0442(1999)012⟨1990:TENOSD⟩2.0.CO;2

Bris, R. L., & Paul, F. (2015). Glacier-specific elevation changes in parts of western Alaska. *Annals of Glaciology*, *56*(70), 184–192. doi: 10.3189/2015AoG70A227

Brun, F., Berthier, E., Wagnon, P., Kääb, A., & Treichler, D. (2017, September). A spatially resolved estimate of High Mountain Asia glacier mass balances from 2000 to 2016. *Nature Geoscience*, *10*(9), 668–673. doi: 10.1038/ngeo2999

Brun, F., Buri, P., Miles, E. S., Wagnon, P., Steiner, J., Berthier, E., ... Pellicciotti,

F. (2016, August). Quantifying volume loss from ice cliffs on debris-covered glaciers using high-resolution terrestrial and aerial photogrammetry. *Journal of Glaciology*, *62*(234), 684–695. doi: 10.1017/jog.2016.54

Brun, F., Wagnon, P., Berthier, E., Shea, J. M., Immerzeel, W. W., Kraaijenbrink, P. D. A., ... Arnaud, Y. (2018, March). *Can ice-cliffs explain the debris-cover anomaly? new insightsfrom Changri Nup Glacier, Nepal, Central Himalaya* (Preprint). Glaciers/Glaciers. doi: 10.5194/tc-2018-38

Burnett, M. G. (2012). *Hexagon (KH-9) mapping camera program and evolution.* Center for the Study of National Reconnaissance.

Carlisle, B. H. (2005). Modelling the Spatial Distribution of DEM Error. *Transactions in GIS*, *9*(4), 521–540. doi: 10.1111/j.1467-9671.2005.00233.x

Casella, G., & Berger, R. L. (2021). *Statistical Inference.* Cengage Learning.

Consortium, R., et al. (2017). Randolph glacier inventory–a dataset of global glacier outlines: Version 6.0. *Global Land Ice Measurements from Space, Colorado, USA, Tech. Rep*.

Cuffey, K. M., & Paterson, W. S. B. (2010). *The Physics of Glaciers.* Academic Press.

Darnell, A. R., Tate, N. J., & Brunsdon, C. (2008, July). Improving user assessment of error implications in digital elevation models. *Computers, Environment and Urban Systems*, *32*(4), 268–277. doi: 10.1016/j.compenvurbsys.2008.02.003

Davis, C., & Ferguson, A. (2004, November). Elevation change of the Antarctic ice sheet, 1995-2000, from ERS-2 satellite radar altimetry. *IEEE Transactions on Geoscience and Remote Sensing*, *42*(11), 2437–2445. doi: 10.1109/TGRS.2004.836789

Dehecq, A., Gardner, A. S., Alexandrov, O., McMichael, S., Hugonnet, R., Shean, D., & Marty, M. (2020). Automated Processing of Declassified KH-9 Hexagon Satellite Images for Global Elevation Change Analysis Since the 1970s. *Frontiers in Earth Science*, *8*, 516. doi: 10.3389/feart.2020.566802

Duethmann, D., Bolch, T., Farinotti, D., Kriegel, D., Vorogushyn, S., Merz, B., ... Güntner, A. (2015). Attribution of streamflow trends in snow and glacier melt-dominated catchments of the Tarim River, Central Asia. *Water Resources Research*, *51*(6), 4727–4750. doi: 10.1002/2014WR016716

Erdoğan, S. (2010, January). Modelling the spatial distribution of DEM error with geographically weighted regression: An experimental study. *Computers & Geosciences*, *36*(1), 34–43. doi: 10.1016/j.cageo.2009.06.005

Falaschi, D., Lenzano, M. G., Villalba, R., Bolch, T., Rivera, A., & Lo Vecchio, A. (2019). Six Decades (1958–2018) of Geodetic Glacier Mass Balance in Monte San Lorenzo, Patagonian Andes. *Frontiers in Earth Science*, *7*, 326. doi: 10.3389/feart.2019.00326

Farr, T. G., Rosen, P. A., Caro, E., Crippen, R., Duren, R., Hensley, S., ... Alsdorf, D. (2007, June). The Shuttle Radar Topography Mission. *Reviews of Geophysics*, *45*(2). doi: 10.1029/2005RG000183

Futamura, N., Takaku, J., Suzuki, H., Iijima, T., Tadono, T., Matsuoka, M., ... Shibasaki, R. (2002, June). High resolution DEM generation from ALOS PRISM data -algorithm development and evaluation. In *IEEE International Geoscience and Remote Sensing Symposium* (Vol. 1, p. 405-407 vol.1). doi: 10.1109/IGARSS.2002.1025054

Gardelle, J., Berthier, E., & Arnaud, Y. (2012). Impact of resolution and radar penetration on glacier elevation changes computed from DEM differencing. *Journal of Glaciology*, *58*(208), 419–422. doi: 10.3189/2012JoG11J175

Gardelle, J., Berthier, E., Arnaud, Y., & Kääb, A. (2013, August). Region-wide glacier mass balances over the Pamir-Karakoram-Himalaya during 1999–2011. *The Cryosphere*, *7*(4), 1263–1286. doi: 10.5194/tc-7-1263-2013

Gardner, A., Moholdt, G., Arendt, A., & Wouters, B. (2012, October). Accel-

erated contributions of Canada's Baffin and Bylot Island glaciers to sea level rise over the past half century. *The Cryosphere*, *6*(5), 1103–1125. doi: 10.5194/tc-6-1103-2012

GDAL/OGR contributors. (2021). *GDAL/OGR geospatial data abstraction software library* [Manual].

Gelman, A., Carlin, J. B., Stern, H. S., Dunson, D. B., Vehtari, A., & Rubin, D. B. (2013). *Bayesian Data Analysis*. CRC Press.

Gelman, A., Vehtari, A., Simpson, D., Margossian, C. C., Carpenter, B., Yao, Y., ... Modrák, M. (2020, November). Bayesian Workflow. *arXiv:2011.01808 [stat]*.

Girod, L., Nuth, C., Kääb, A., McNabb, R., & Galland, O. (2017, July). MMASTER: Improved ASTER DEMs for Elevation Change Monitoring. *Remote Sensing*, *9*(7), 704. doi: 10.3390/rs9070704

González-Moradas, M. d. R., & Viveen, W. (2020, February). Evaluation of ASTER GDEM2, SRTMv3.0, ALOS AW3D30 and TanDEM-X DEMs for the Peruvian Andes against highly accurate GNSS ground control points and geomorphological-hydrological metrics. *Remote Sensing of Environment*, *237*, 111509. doi: 10.1016/j.rse.2019.111509

Guillet, G., Guillet, T., & Ravanel, L. (2020, January). Camera orientation, calibration and inverse perspective with uncertainties: A Bayesian method applied to area estimation from diverse photographs. *ISPRS Journal of Photogrammetry and Remote Sensing*, *159*, 237–255. doi: 10.1016/j.isprsjprs.2019.11.013

Guillet, G., King, O., Lv, M., Ghuffar, S., Benn, D., Quincey, D., & Bolch, T. (2021, October). A regionally resolved inventory of High Mountain Asia surge-type glaciers, derived from a multi-factor remote sensing approach. *The Cryosphere Discussions*, 1–31. doi: 10.5194/tc-2021-303

Guo, L., Li, J., Li, Z.-w., Wu, L.-x., Li, X., Hu, J., ... Li, Z.-q. (2020). The Surge of the Hispar Glacier, Central Karakoram: SAR 3-D Flow Velocity Time Series and Thickness Changes. *Journal of Geophysical Research: Solid Earth*, *125*(7), e2019JB018945. doi: 10.1029/2019JB018945

Hamill, T. M., Whitaker, J. S., & Snyder, C. (2001, November). Distance-Dependent Filtering of Background Error Covariance Estimates in an Ensemble Kalman Filter. *Monthly Weather Review*, *129*(11), 2776–2790. doi: 10.1175/1520-0493(2001)129⟨2776:DDFOBE⟩2.0.CO;2

Holmes, K. W., Chadwick, O. A., & Kyriakidis, P. C. (2000, June). Error in a USGS 30-meter digital elevation model and its impact on terrain modeling. *Journal of Hydrology*, *233*(1), 154–173. doi: 10.1016/S0022-1694(00)00229-8

Horowitz, E., & Papa, M. (1992, January). Polygon Clipping: Analysis and Experiences. In J. D. Ullman (Ed.), *Theoretical Studies in Computer Science* (pp. 315–339). Academic Press. doi: 10.1016/B978-0-12-708240-0.50016-2

Hubacek, M., Kovarik, V., & Kratochvil, V. (2016, June). Analysis of Influences of Terrain Relief Roughness on DEM accuracy Generated fom Lida in the Czech Republic Territory. In *The International Archives of the Photogrammetry, Remote Sensing and Spatial Information Sciences* (Vol. XLI-B4, pp. 25–30). Copernicus GmbH. doi: 10.5194/isprs-archives-XLI-B4-25-2016

Hugonnet, R., McNabb, R., Berthier, E., Menounos, B., Nuth, C., Girod, L., ... Kääb, A. (2021, April). Accelerated global glacier mass loss in the early twenty-first century. *Nature*, *592*(7856), 726–731. doi: 10.1038/s41586-021-03436-z

Hunter, G. J., & Goodchild, M. F. (1997). Modeling the Uncertainty of Slope and Aspect Estimates Derived from Spatial Databases. *Geographical Analysis*, *29*(1), 35–49. doi: 10.1111/j.1538-4632.1997.tb00944.x

Huss, M. (2013, May). Density assumptions for converting geodetic glacier volume change to mass change. *The Cryosphere*, *7*(3), 877–887. doi: 10.5194/tc-7-877-2013

Immerzeel, W. W., Pellicciotti, F., & Shrestha, A. B. (2012, February). Glaciers

as a Proxy to Quantify the Spatial Distribution of Precipitation in the Hunza Basin. *Mountain Research and Development*, *32*(1), 30–38. doi: 10.1659/MRD-JOURNAL-D-11-00097.1

Jacobsen, K. (2016, June). Analysis and Correction of Systematic Height Model Erros. *ISPRS - International Archives of the Photogrammetry, Remote Sensing and Spatial Information Sciences*, *XLI-B1*, 333–339. doi: 10.5194/isprsarchives-XLI-B1-333-2016

Jakob, L., Gourmelen, N., Ewart, M., & Plummer, S. (2021, April). Spatially and temporally resolved ice loss in High Mountain Asia and the Gulf of Alaska observed by CryoSat-2 swath altimetry between 2010 and 2019. *The Cryosphere*, *15*(4), 1845–1862. doi: 10.5194/tc-15-1845-2021

Janowski, L., Tylmann, K., Trzcinska, K., Rudowski, S., & Tegowski, J. (2021). Exploration of Glacial Landforms by Object-Based Image Analysis and Spectral Parameters of Digital Elevation Model. *IEEE Transactions on Geoscience and Remote Sensing*, 1–17. doi: 10.1109/TGRS.2021.3091771

Jiskoot, H. (2011). Glacier surging. *Encyclopedia of Snow, Ice and Glaciers*, 415–428.

Kaab, A. (2008, October). Glacier Volume Changes Using ASTER Satellite Stereo and ICESat GLAS Laser Altimetry. A Test Study on EdgeØya, Eastern Svalbard. *IEEE Transactions on Geoscience and Remote Sensing*, *46*(10), 2823–2830. doi: 10.1109/TGRS.2008.2000627

Kargel, J. S., Leonard, G. J., Wheate, R. D., & Edwards, B. (2014). ASTER and DEM Change Assessment of Glaciers Near Hoodoo Mountain, British Columbia, Canada. In J. S. Kargel, G. J. Leonard, M. P. Bishop, A. Kääb, & B. H. Raup (Eds.), *Global Land Ice Measurements from Space* (pp. 353–373). Berlin, Heidelberg: Springer. doi: 10.1007/978-3-540-79818-7_15

Kim, K., Jezek, K. C., & Liu, H. (2007, December). Orthorectified image mosaic of Antarctica from 1963 Argon satellite photography: Image processing and glaciological applications. *International Journal of Remote Sensing*, *28*(23), 5357–5373. doi: 10.1080/01431160601105850

King, O., Bhattacharya, A., & Bolch, T. (2021, June). The presence and influence of glacier surging around the Geladandong ice caps, North East Tibetan Plateau. *Advances in Climate Change Research*, *12*(3), 299–312. doi: 10.1016/j.accre.2021.05.001

King, O., Bhattacharya, A., Ghuffar, S., Tait, A., Guilford, S., Elmore, A. C., & Bolch, T. (2020, November). Six Decades of Glacier Mass Changes around Mt. Everest Are Revealed by Historical and Contemporary Images. *One Earth*, *3*(5), 608–620. doi: 10.1016/j.oneear.2020.10.019

Kyriakidis, P. C., Shortridge, A. M., & Goodchild, M. F. (1999, October). Geostatistics for conflation and accuracy assessment of digital elevation models. *International Journal of Geographical Information Science*, *13*(7), 677–707. doi: 10.1080/136588199241067

Lehmann, E. L., & Casella, G. (2006). *Theory of Point Estimation*. Springer Science & Business Media.

Leinss, S., & Bernhard, P. (2021). TanDEM-X:deriving InSAR Height Changes and Velocity Dynamics of Great Aletsch Glacier. *IEEE Journal of Selected Topics in Applied Earth Observations and Remote Sensing*, *14*, 4798–4815. doi: 10.1109/JSTARS.2021.3078084

Li, J., & Heap, A. D. (2014, March). Spatial interpolation methods applied in the environmental sciences: A review. *Environmental Modelling & Software*, *53*, 173–189. doi: 10.1016/j.envsoft.2013.12.008

Liu, H., & Jezek, K. C. (1999). Investigating DEM Error Patterns by Directional Variograms and Fourier Analysis. *Geographical Analysis*, *31*(3), 249–266. doi: 10.1111/j.1538-4632.1999.tb00981.x

Mayr, E., Hagg, W., Mayer, C., & Braun, L. (2013, January). Calibrating a spa-

tially distributed conceptual hydrological model using runoff, annual mass balance and winter mass balance. *Journal of Hydrology*, *478*, 40–49. doi: 10.1016/j.jhydrol.2012.11.035

McNabb, R., Nuth, C., Kääb, A., & Girod, L. (2019, March). Sensitivity of glacier volume change estimation to DEM void interpolation. *The Cryosphere*, *13*(3), 895–910. doi: 10.5194/tc-13-895-2019

Mertes, J. R., Gulley, J. D., Benn, D. I., Thompson, S. S., & Nicholson, L. I. (2017). Using structure-from-motion to create glacier DEMs and orthoimagery from historical terrestrial and oblique aerial imagery. *Earth Surface Processes and Landforms*, *42*(14), 2350–2364. doi: 10.1002/esp.4188

Moholdt, G., & Kääb, A. (2012, January). A new DEM of the Austfonna ice cap by combining differential SAR interferometry with ICESat laser altimetry. *Polar Research*, *31*(1), 18460. doi: 10.3402/polar.v31i0.18460

Mölg, N., & Bolch, T. (2017, October). Structure-from-Motion Using Historical Aerial Images to Analyse Changes in Glacier Surface Elevation. *Remote Sensing*, *9*(10), 1021. doi: 10.3390/rs9101021

Monckton, C. (1994). An Investigation into the spatial structure of error in digital elevation data. In *Innovations In GIS*. CRC Press.

Mukherjee, S., Mukherjee, S., Garg, R. D., Bhardwaj, A., & Raju, P. L. N. (2013, June). Evaluation of topographic index in relation to terrain roughness and DEM grid spacing. *Journal of Earth System Science*, *122*(3), 869–886. doi: 10.1007/s12040-013-0292-0

Mukhopadhyay, B., & Khan, A. (2016, February). Altitudinal variations of temperature, equilibrium line altitude, and accumulation-area ratio in Upper Indus Basin. *Hydrology Research*, *48*(1), 214–230. doi: 10.2166/nh.2016.144

Muskett, R. R., Lingle, C. S., Sauber, J. M., Post, A. S., Tangborn, W. V., Rabus, B. T., & Echelmeyer, K. A. (2009). Airborne and spaceborne DEM- and laser altimetry-derived surface elevation and volume changes of the Bering Glacier system, Alaska, USA, and Yukon, Canada, 1972–2006. *Journal of Glaciology*, *55*(190), 316–326. doi: 10.3189/002214309788608750

Nakawo, M., & Young, G. J. (1981). Field Experiments to Determine the Effect of a Debris Layer on Ablation of Glacier Ice. *Annals of Glaciology*, *2*, 85–91. doi: 10.3189/172756481794352432

NASA, L. D. (2013). NASA shuttle radar topography mission (SRTM) version 3.0 (SRTM plus) product release. Land process distributed active archive center. *National Aeronautics and Space Administration*.

Neckel, N., Kropáček, J., Bolch, T., & Hochschild, V. (2014, January). Glacier mass changes on the Tibetan Plateau 2003–2009 derived from ICESat laser altimetry measurements. *Environmental Research Letters*, *9*(1), 014009. doi: 10.1088/1748-9326/9/1/014009

Nicholson, L., & Benn, D. I. (2006). Calculating ice melt beneath a debris layer using meteorological data. *Journal of Glaciology*, *52*(178), 463–470. doi: 10.3189/172756506781828584

Nikolakopoulos, K. G. (2020, July). Accuracy assessment of ALOS AW3D30 DSM and comparison to ALOS PRISM DSM created with classical photogrammetric techniques. *European Journal of Remote Sensing*, *53*(sup2), 39–52. doi: 10.1080/22797254.2020.1774424

Nilsson, J., Sandberg Sørensen, L., Barletta, V. R., & Forsberg, R. (2015, January). Mass changes in Arctic ice caps and glaciers: Implications of regionalizing elevation changes. *The Cryosphere*, *9*(1), 139–150. doi: 10.5194/tc-9-139-2015

Noh, M.-J., & Howat, I. M. (2015, March). Automated stereo-photogrammetric DEM generation at high latitudes: Surface Extraction with TIN-based Search-space Minimization (SETSM) validation and demonstration over glaciated regions. *GIScience & Remote Sensing*, *52*(2), 198–217. doi: 10.1080/15481603.2015.1008621

Nuth, C., & Kääb, A. (2011, March). Co-registration and bias corrections of satellite elevation data sets for quantifying glacier thickness change. *The Cryosphere*, *5*(1), 271–290. doi: 10.5194/tc-5-271-2011

Oksanen, J., & Sarjakoski, T. (2005, October). Error propagation of DEM-based surface derivatives. *Computers & Geosciences*, *31*(8), 1015–1027. doi: 10.1016/j.cageo.2005.02.014

Pandey, P., Kulkarni, A. V., & Venkataraman, G. (2013, July). Remote sensing study of snowline altitude at the end of melting season, Chandra-Bhaga basin, Himachal Pradesh, 1980–2007. *Geocarto International*, *28*(4), 311–322. doi: 10.1080/10106049.2012.705336

Papasodoro, C., Berthier, E., Royer, A., Zdanowicz, C., & Langlois, A. (2015, August). Area, elevation and mass changes of the two southernmost ice caps of the Canadian Arctic Archipelago between 1952 and 2014. *The Cryosphere*, *9*(4), 1535–1550. doi: 10.5194/tc-9-1535-2015

Paul, F., Bolch, T., Briggs, K., Kääb, A., McMillan, M., McNabb, R., ... Wuite, J. (2017, December). Error sources and guidelines for quality assessment of glacier area, elevation change, and velocity products derived from satellite data in the Glaciers_cci project. *Remote Sensing of Environment*, *203*, 256–275. doi: 10.1016/j.rse.2017.08.038

Paul, F., Strozzi, T., Schellenberger, T., & Kääb, A. (2017, September). The 2015 Surge of Hispar Glacier in the Karakoram. *Remote Sensing*, *9*(9), 888. doi: 10.3390/rs9090888

Pieczonka, T., & Bolch, T. (2015, May). Region-wide glacier mass budgets and area changes for the Central Tien Shan between ˜1975 and 1999 using Hexagon KH-9 imagery. *Global and Planetary Change*, *128*, 1–13. doi: 10.1016/j.gloplacha.2014.11.014

Pieczonka, T., Bolch, T., Junfeng, W., & Shiyin, L. (2013, March). Heterogeneous mass loss of glaciers in the Aksu-Tarim Catchment (Central Tien Shan) revealed by 1976 KH-9 Hexagon and 2009 SPOT-5 stereo imagery. *Remote Sensing of Environment*, *130*, 233–244. doi: 10.1016/j.rse.2012.11.020

Podgórski, J., Kinnard, C., Petlicki, M., & Urrutia, R. (2019, January). Performance Assessment of TanDEM-X DEM for Mountain Glacier Elevation Change Detection. *Remote Sensing*, *11*(2), 187. doi: 10.3390/rs11020187

Pratap, B., Dobhal, D. P., Mehta, M., & Bhambri, R. (2015). Influence of debris cover and altitude on glacier surface melting: A case study on Dokriani Glacier, central Himalaya, India. *Annals of Glaciology*, *56*(70), 9–16. doi: 10.3189/2015AoG70A971

Quincey, D. J., & Luckman, A. (2014, April). Brief Communication: On the magnitude and frequency of Khurdopin glacier surge events. *The Cryosphere*, *8*(2), 571–574. doi: 10.5194/tc-8-571-2014

Ragettli, S., Bolch, T., & Pellicciotti, F. (2016, September). Heterogeneous glacier thinning patterns over the last 40 years in Langtang Himal, Nepal. *The Cryosphere*, *10*(5), 2075–2097. doi: 10.5194/tc-10-2075-2016

Rankl, M., & Braun, M. (2016, March). Glacier elevation and mass changes over the central Karakoram region estimated from TanDEM-X and SRTM/X-SAR digital elevation models. *Annals of Glaciology*, *57*(71), 273–281. doi: 10.3189/2016AoG71A024

Rashid, I., Abdullah, T., Glasser, N. F., Naz, H., & Romshoo, S. A. (2018, February). Surge of Hispar Glacier, Pakistan, between 2013 and 2017 detected from remote sensing observations. *Geomorphology*, *303*, 410–416. doi: 10.1016/j.geomorph.2017.12.018

Raup, B. H., Andreassen, L. M., Bolch, T., & Bevan, S. (2015). Remote sensing of glaciers. *Remote Sensing of the Cryosphere*, 123–56.

Ruggiero, G. A., Cosme, E., Brankart, J.-M., Sommer, J. L., & Ubelmann, C. (2016, December). An Efficient Way to Account for Observation Error Correlations

in the Assimilation of Data from the Future SWOT High-Resolution Altimeter Mission. *Journal of Atmospheric and Oceanic Technology*, *33*(12), 2755–2768. doi: 10.1175/JTECH-D-16-0048.1

Sang, H., & Huang, J. Z. (2012). A full scale approximation of covariance functions for large spatial data sets. *Journal of the Royal Statistical Society: Series B (Statistical Methodology)*, *74*(1), 111–132. doi: 10.1111/j.1467-9868.2011.01007.x

Sapiano, J. J., Harrison, W. D., & Echelmeyer, K. A. (1998). Elevation, volume and terminus changes of nine glaciers in North America. *Journal of Glaciology*, *44*(146), 119–135. doi: 10.3189/S0022143000002410

Schwitter, M. P., & Raymond, C. F. (1993). Changes in the longitudinal profiles of glaciers during advance and retreat. *Journal of Glaciology*, *39*(133), 582–590. doi: 10.3189/S0022143000016476

Shangguan, D. H., Bolch, T., Ding, Y. J., Kröhnert, M., Pieczonka, T., Wetzel, H. U., & Liu, S. Y. (2015, April). Mass changes of Southern and Northern Inylchek Glacier, Central Tian Shan, Kyrgyzstan, during ∼1975 and 2007 derived from remote sensing data. *The Cryosphere*, *9*(2), 703–717. doi: 10.5194/tc-9-703-2015

Shean, D. E., Joughin, I. R., Dutrieux, P., Smith, B. E., & Berthier, E. (2019, October). Ice shelf basal melt rates from a high-resolution digital elevation model (DEM) record for Pine Island Glacier, Antarctica. *The Cryosphere*, *13*(10), 2633–2656. doi: 10.5194/tc-13-2633-2019

Simonsen, S. B., Barletta, V. R., Colgan, W. T., & Sørensen, L. S. (2021). Greenland Ice Sheet Mass Balance (1992–2020) From Calibrated Radar Altimetry. *Geophysical Research Letters*, *48*(3), e2020GL091216. doi: 10.1029/2020GL091216

Sutherland, I. E., & Hodgman, G. W. (1974, January). Reentrant polygon clipping. *Communications of the ACM*, *17*(1), 32–42. doi: 10.1145/360767.360802

Toutin, T. (2008, April). ASTER DEMs for geomatic and geoscientific applications: A review. *International Journal of Remote Sensing*, *29*(7), 1855–1875. doi: 10.1080/01431160701408477

Truffer, M., Kääb, A., Harrison, W. D., Osipova, G. B., Nosenko, G. A., Espizua, L., ... Lai, A. W. (2021, January). Chapter 13 - Glacier surges. In W. Haeberli & C. Whiteman (Eds.), *Snow and Ice-Related Hazards, Risks, and Disasters (Second Edition)* (pp. 417–466). Elsevier. doi: 10.1016/B978-0-12-817129-5.00003-2

Vijay, S., & Braun, M. (2018, June). Early 21st century spatially detailed elevation changes of Jammu and Kashmir glaciers (Karakoram–Himalaya). *Global and Planetary Change*, *165*, 137–146. doi: 10.1016/j.gloplacha.2018.03.014

Vincent, C., Wagnon, P., Shea, J. M., Immerzeel, W. W., Kraaijenbrink, P., Shrestha, D., ... Sherpa, S. F. (2016, August). Reduced melt on debris-covered glaciers: Investigations from Changri Nup Glacier, Nepal. *The Cryosphere*, *10*(4), 1845–1858. doi: 10.5194/tc-10-1845-2016

Wang, D., & Kääb, A. (2015, August). Modeling Glacier Elevation Change from DEM Time Series. *Remote Sensing*, *7*(8), 10117–10142. doi: 10.3390/rs70810117

Wang, K., & Zhang, T. (2015, December). Gauss-Newton method for DEM co-registration. In *International Conference on Intelligent Earth Observing and Applications 2015* (Vol. 9808, p. 98080M). International Society for Optics and Photonics. doi: 10.1117/12.2207244

Wechsler, S. P., & Kroll, C. N. (2006, September). Quantifying DEM Uncertainty and its Effect on Topographic Parameters. *Photogrammetric Engineering & Remote Sensing*, *72*(9), 1081–1090. doi: 10.14358/PERS.72.9.1081

Weng, Q. (2006). An Evaluation of Spatial Interpolation Accuracy of Elevation Data. In A. Riedl, W. Kainz, & G. A. Elmes (Eds.), *Progress in Spatial Data*

Handling: 12th International Symposium on Spatial Data Handling (pp. 805–824). Berlin, Heidelberg: Springer. doi: 10.1007/3-540-35589-8_50

Wheate, R. D., Berthier, E., Bolch, T., Menounos, B. P., Shea, J. M., Clague, J. J., & Schiefer, E. (2014). Remote Sensing of Glaciers in the Canadian Cordillera, Western Canada. In J. S. Kargel, G. J. Leonard, M. P. Bishop, A. Kääb, & B. H. Raup (Eds.), *Global Land Ice Measurements from Space* (pp. 333–352). Berlin, Heidelberg: Springer. doi: 10.1007/978-3-540-79818-7_14

Whitehead, K., Moorman, B. J., & Hugenholtz, C. H. (2013, December). Brief Communication: Low-cost, on-demand aerial photogrammetry for glaciological measurement. *The Cryosphere*, *7*(6), 1879–1884. doi: 10.5194/tc-7-1879-2013

Wijngaard, R. R., Steiner, J. F., Kraaijenbrink, P. D. A., Klug, C., Adhikari, S., Banerjee, A., ... Immerzeel, W. W. (2019). Modeling the Response of the Langtang Glacier and the Hintereisferner to a Changing Climate Since the Little Ice Age. *Frontiers in Earth Science*, *0*. doi: 10.3389/feart.2019.00143

Wise, S. (2011, August). Cross-validation as a means of investigating DEM interpolation error. *Computers & Geosciences*, *37*(8), 978–991. doi: 10.1016/j.cageo.2010.12.002

Zhang, R., Fattahi, S., & Sojoudi, S. (2018, July). Large-Scale Sparse Inverse Covariance Estimation via Thresholding and Max-Det Matrix Completion. In *International Conference on Machine Learning* (pp. 5766–5775). PMLR.

Acknowledgments

We thank Dr. Owen King for his constructive comments during the writing of this manuscript. This study was supported by the Strategic Priority Research Program of Chinese Academy of Sciences (XDA20100300) and the Swiss National Science Foundation (200021E_177652/1) within the within the framework of the Research Unit GlobalCDA funded by Deutsche Forschngsgemeinschaft (grant no. FOR2630).